

Multi-Wavelength and Multi-Instrument Observations of Flows and Magnetic Fields in a Complex Sunspot

Bachelorarbeit
zur Erlangung des akademischen Grades
Bachelor of Science (B.Sc.)
in der Wissenschaftsdisziplin Physik

eingereicht an der
Mathematisch-Naturwissenschaftlichen Fakultät I
Institut für Physik
Humboldt-Universität zu Berlin

Betreuung:
Herr Prof. Dr. Marek Kowalski
Herr apl. Prof. Dr. Carsten Denker

eingereicht am: 4. Mai 2016

Felicitas Böhm
geb. 16. September 1990 in Berlin
Matrikelnummer: 532107



Leibniz-Institut für Astrophysik Potsdam
An der Sternwarte 16
14482 Potsdam

Table of Contents

Zusammenfassung	1
Abstract	2
1 Introduction	3
1.1 Sunspots	3
1.1.1 Solar Atmosphere	3
1.1.2 General Properties of Sunspots	4
1.1.3 Solar Cycle	4
1.1.4 Structure of Umbra and Penumbra	5
1.1.5 Wilson Depression	6
1.1.6 Evershed Flow	7
1.1.7 Growth of an Active Region	7
1.1.8 Decay of an Active Region	8
1.2 Spectral Lines	8
1.2.1 Kirchhoff's Laws	8
1.2.2 Profiles of Spectral Lines	9
1.3 Polarimetry	9
1.3.1 Zeeman Splitting	9
1.3.2 Polarized Light	10
2 Instruments	12
2.1 Solar Dynamics Observatory	12
2.1.1 Atmospheric Imaging Assembly	12
2.1.2 Helioseismic and Magnetic Imager	13
2.2 GREGOR Solar Telescope	14
2.2.1 Telescope Design	14
2.2.2 GREGOR Infrared Spectrograph	15
2.2.3 Polarimeter	15
2.3 Interface Region Imaging Spectrograph (IRIS)	16
2.3.1 Overview and Mission Details	16
2.3.2 Telescope	16
2.3.3 Spectrograph and Slit-Jaw Imager	16
2.3.4 Detectors	17
3 Observations	18
3.1 Overview	18
3.2 Temporal Evolution	20
3.2.1 Photometric and Magnetic Evolution	20
3.2.2 Temporal Evolution of Solar Activity	21
4 Results	22
4.1 Basic Data Reduction and Pre-Processing	22
4.1.1 Basic Data Reduction	22
4.1.2 Pre-Processing	23
4.2 Maps of Physical Parameters	27
4.2.1 Fitting Models	27

4.2.2	Physical Maps	29
4.2.3	Experimental Errors and Error Analysis	31
4.3	Outlook	33
5	Conclusions	34
	Bibliography	35
	Acknowledgments	39
	Appendix A – List of Acronyms	40
	Appendix B – List of Programs	41

Zusammenfassung

Erruptionen auf der Sonne, wie Strahlungsausbrüche, haben ihren Ursprung in aktiven Regionen. Sie sind in der Lage, die Erde und ihre unmittelbare Umgebung zu beeinflussen und können z.B. Funkverbindungen unterbrechen. Da Sonnenflecken einen bedeutenden Teil dieser aktiven Regionen ausmachen, sind sie ein populäres Forschungsgebiet. Um die aktiven Regionen auf der Sonne vollständig verstehen zu können, müssen Sonnenflecken eingehender untersucht werden.

Um den Ursprung und die Entwicklung von aktiven Regionen bestimmen zu können, werden präzise Messungen der dreidimensionalen Magnet- und Strömungsfelder in der Photosphäre und Chromosphäre benötigt. Ein vollständiges Bild von der Entwicklung aktiver Regionen wird erlangt durch eine Verbindung aus hochauflösenden und synoptischen Beobachtungen. Im August 2015 wurden solche Messungen im Rahmen einer zehn Tage andauernden koordinierten Kampagne ausgeführt. Auf dem Boden ausgeführte Beobachtungen mit dem GREGOR Sonnenteleskop und dem Vakuum-Turm-Teleskop (VTT) am Observatorio del Teide auf Teneriffa wurden ergänzt mit Daten von den Weltraummissionen Hinode, Solar Dynamics Observatory (SDO) und Interface Region Imaging Spectrograph (IRIS). Die Instrumente lieferten Beobachtungen von hochauflösenden Vektor-Magnetogrammen und dreidimensionalen Strömungsfeldern.

Diese Arbeit gibt zunächst eine Einleitung in die Charakteristiken von aktiven Regionen auf der Sonne, insbesondere in die von Sonnenflecken. Eigenschaften und Aufbau von Sonnenflecken, Wilson-Effekt, Evershed-Effekt und die Entwicklung von aktiven Regionen werden dargestellt. Anschließend werden die wichtigsten Instrumente beschrieben, mit denen die Daten aufgenommen wurden. Zur Analyse der aktiven Region NOAA 12396 (vom National Oceanic and Atmospheric Administration (NOAA) zugewiesene Nummer) wird einer der Datensätze und die Resultate der Beobachtungen vom 6. August 2015 mit dem GREGOR Infrarot Spektrographen (GRIS) präsentiert. Die Daten beinhalten vier spektrale Stokes IQUV Profile der photosphärischen Linien Si I 1082.7 nm und Ca I 1082.9 nm, zusammen mit der chromosphärischen Linie He I 1083.0 nm. Die Beobachtungen waren auf den östlichen Teil der aktiven Region NOAA 12396 gerichtet, welcher zwei Sonnenflecken mit negativer Polarität und eine Pore enthielt. Daten von SDO und IRIS ergänzen die vom Boden ausgeführten GREGOR Beobachtungen.

Um einen Überblick über die aktive Region zu bekommen, wurden sowohl Kontinuumsbilder und Magnetogramme entlang der Sichtlinie vom SDO, als auch Spaltbilder von IRIS benutzt. Genauer gesagt, wurden die photometrische und magnetische Entwicklung der Sonnenflecken den SDO Daten entnommen, während die IRIS Daten dazu dienten, die Struktur in der Übergangsregion zwischen Chromosphäre und Korona zu visualisieren. Um den östlichen Teil der aktiven Region näher zu betrachten, wurden die spektropolarimetrischen Daten von GRIS zunächst sorgfältig kalibriert. Anschließend wurden mit Hilfe der kalibrierten spektralen Profile Karten erstellt, die diverse physikalische Parameter visualisieren, wie z.B. die Kontinuumsintensität, vorzeichenbehaftete Stokes-V Profile und lineare und zirkulare Polarisation. Die Geschwindigkeiten entlang der Sichtlinie in der Photosphäre und Chromosphäre wurden jeweils den Si I, Ca I und He I Linien entnommen.

Abstract

Solar explosive events, such as flares, occur in active regions and are able to influence the Earth and the near-Earth environment, e.g., being able to disrupt radiocommunications. Since sunspots are a main feature of those active regions, they are a prominent subject of research. A close investigation of sunspots is needed to attain a complete understanding of the Sun's active regions.

For a precise determination of the origin and evolution of active regions, accurate measurements of the photospheric and chromospheric three-dimensional magnetic and flow fields are required. A comprehensive picture of active region development can be obtained by a combination of high-resolution and synoptic observations. In August 2015, such measurements were carried out in a coordinated campaign, lasting for ten days. Ground-based observations from the GREGOR solar telescope and the Vacuum Tower Telescope (VTT) at Observatorio del Teide, Tenerife were complemented by data from space mission Hinode, Solar Dynamics Observatory (SDO), and Interface Region Imaging Spectrograph (IRIS), yielding high-resolution vector magnetograms and three-dimensional flow field observations.

This thesis first gives an introduction into the characteristics of active regions on the Sun, focusing on sunspots. General properties and structure of sunspots, Wilson depression, Evershed flow, as well as the evolution of active regions are delineated. Then, the main instruments used to obtain the data are described. To analyse the active region NOAA 12396 (number designated by the National Oceanic and Atmospheric Administration (NOAA)), one of the datasets and results of observations taken on 2015 August 6, from the GREGOR Infrared Spectrograph (GRIS), are presented, which includes four Stokes IQUV spectral profiles in Si I 1082.7 nm and Ca I 1082.9 nm (photosphere), together with He I 1083.0 nm (chromosphere). These observations focused on the trailing part of active region NOAA 12396, which consisted of two negative polarity sunspots and a pore. Data from SDO and IRIS complement the ground-based GREGOR observations.

To obtain an overview of the active region, continuum images and line-of-sight (LOS) magnetograms from SDO along with slit-jaw images from IRIS are used. In detail, the photometric and magnetic evolution of the sunspots was extracted from SDO data, whereas IRIS data were used to visualize the structure in the transition region. Focusing on the trailing part of the active region, GRIS spectropolarimetric data were first carefully calibrated. Afterwards, maps depicting various physical parameters such as continuum intensity, signed Stokes-V profiles, linear and circular polarizations, among others, were created from the calibrated spectral profiles. The LOS velocities in photosphere and chromosphere were inferred from Si I, Ca I, and He I line, respectively.

Chapter 1

Introduction

1.1 Sunspots

The Sun fascinated humans throughout history. Mentions of sunspots reach back to ancient Greece as far as 325 BC, where Theophrastus of Athens first writes about dark spots on the Sun as a sign for rain. Probably the first one to glimpse sunspots through a telescope was Galileo Galilei in 1610. Since then instruments for solar observations and their resolving power improved giving more and more detailed information about the Sun and the dark spots covering its surface (Thomas and Weiss, 2008).

1.1.1 Solar Atmosphere

Observations of sunspots focus on the solar atmosphere, which consists of three main layers, the photosphere, the chromosphere, and the corona. The atmosphere extends many solar radii into space. The fact that different ranges of the solar spectrum originate from different layers of the Sun's atmosphere allows to observe them separately (Zirker, 2002).

The photosphere is the “surface” of the Sun, although it is not firm, but it is a boundary between the dense interior and the tenuous atmospheric layers above. Nearly all of the Sun's energy is radiated into space from this layer, giving the photosphere its name. Using Wien's displacement law, the temperature of the photosphere seen as a black body can be calculated to be around 5770 K (Zirker, 2002). Depending on which opacity is chosen to define the top of the photosphere, its depth ranges between 400–500 km (Mullan, 2010).

The chromosphere lies above the photosphere, and it can be seen for a short period of time right before and after a total solar eclipse, when the photosphere is covered by the lunar disc, since its intensity only reaches only about 10^{-4} of the photosphere's value. The chromosphere spans upwards for around 1600 km, with the temperature increasing with altitude from 4400 K to 10 000 K. There are not only absorption but also emission lines produced in this region (see Sect. 1.2 for the explanation), particularly $H\alpha$, which is often used for observations of the chromosphere. Its appearance is dominated by supergranulation and so called spicules, vertical gas filaments with lifetimes of 15 min extending up to 10 000 km (Carroll and Ostlie, 2007).

Between chromosphere and corona lies a zone called “transition region”, which represents a specific temperature regime. From chromosphere to corona, temperatures jump abruptly from 10^4 K to 10^6 K and the border where that happens is called the transition zone. To investigate the transition region, observations from space, focusing on the ultraviolet spectrum from 50–160 nm, are needed (Stix, 2002).

The outermost region of the solar atmosphere is the corona, which extends into space irregularly. Temperatures reach about 10^6 K, which is evidently higher than photospheric temperatures, and the so called coronal heating is still object of research today. Due to the high temperatures, the Sun's gravity cannot hold the gas of the corona and it escapes into space as solar wind. Coronal features are coronal holes, dark regions often located at the Sun's poles, and associated with open magnetic field lines, as well as coronal loops, found around sunspots and active regions, which are related to closed magnetic lines (Mullan, 2010).

DAILY SUNSPOT AREA AVERAGED OVER INDIVIDUAL SOLAR ROTATIONS

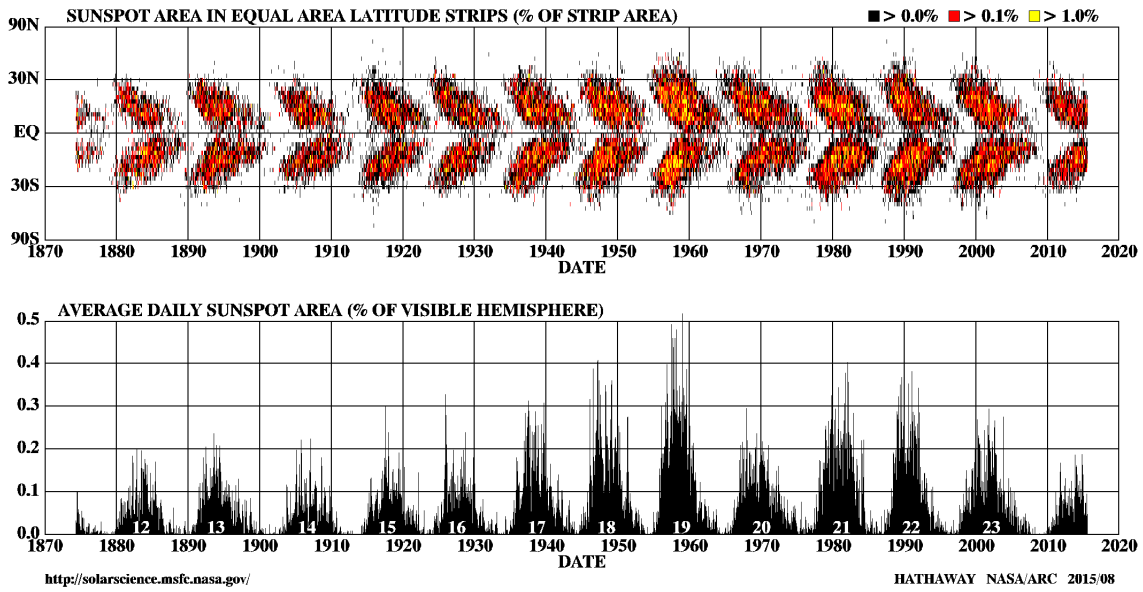


Figure 1.1: Butterfly diagram (top) illustrating the 11-year cycle and the proportion of the area of the solar disc covered by sunspots (bottom). (2016-05-03 – <http://solarscience.msfc.nasa.gov/images/bfly.gif>)

1.1.2 General Properties of Sunspots

Sunspots appear as dark spots on the solar disc. They are visible in the photosphere and contain strong magnetic fields. Sizes of sunspots range widely, the smallest have diameters of only 3500 km, while the largest ones may exceed 60 000 km (Thomas and Weiss, 2008). Typical are diameters of about 10 000 km (Foukal, 2013). The largest sunspot observed appeared in March 1947 with a mean diameter of 130 000 km and an area of $4300 \times 10^{-6} A_{\odot/2}$ with $A_{\odot/2} = 2\pi R_{\odot}^2$ being the surface of the visible solar hemisphere (Newton, 1955; Abetti, 1957).

Sunspots consist of a inner, darker region called umbra and a somewhat brighter region around the umbra, the penumbra. Spots without penumbra are called pores and might later develop into sunspots. The umbra occupies about 18% of the sunspot’s area and 40% of its radius (Thomas and Weiss, 2008). Umbrae typically radiate 20–30% of the flux of the quiet Sun and therefore are cooler by about 1000–1900 K. Penumbrae are brighter, resulting in only 250–400 K difference to the quiet Sun at the photosphere. The reduced temperatures in sunspots are caused by the magnetic field. The strong field partially suppresses convection and thus blocks the energy transport. Magnetic field strengths in the umbra are typically around 2800 G. The field is almost vertical in the center, becoming more and more horizontal towards the edge of the spot. At the outer boarder of the penumbra the field strength drops to less than 1000 G and the inclination of the field lines is 70° on average (Thomas and Weiss, 2008).

Sunspots often appear as pairs or even in groups. They are carried across the solar disc by solar rotation, and because they are mainly east-west oriented, they are called leading / preceding and following / trailing spots. In additon to solar rotation, sunspots can show motions of their own, i.e., sunspot rotation or even splitting (Louis *et al.*, 2014).

1.1.3 Solar Cycle

Long lasting studies of sunspots on the solar disc indicate that their number varies significantly and does so periodically (Hathaway, 2015). To be able to measure and compare the number of sunspots from different observations, Rudolf Wolf defined the Zurich Sunspot Number

$$R_z = k(10g + f). \quad (1.1)$$

The number of sunspot groups visible is g , f is the number of individual spots, and k is a correction factor for different observers, sites, and telescopes. If R_z is very small or even zero for several months, the solar

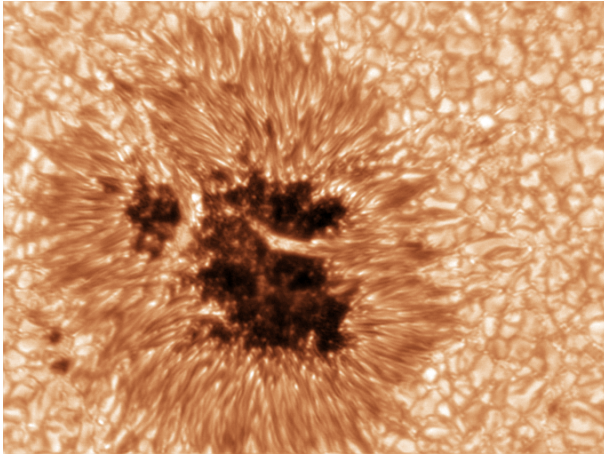


Figure 1.2: Sunspot observed with the GREGOR solar telescope. The umbra with a light-bridge as well as the detailed structure of penumbral filaments can be seen. (2016-04-14 – gregor.aip.de)

cycle is at the “solar minimum”. For the “solar maximum” R_z reaches 100–200 (Mullan, 2010). The solar cycle was first noticed by Heinrich Schwabe, and it lasts for 11 years on average, but this time span may vary by about a year (Schwabe, 1843).

Not only the number of sunspots present on the solar disc varies with the solar cycle, but also the latitudes at which the spots appear. At the beginning of a new cycle, spots appear in the “activity belt” at $30^\circ - 35^\circ$ latitude in both hemispheres. During the cycle, spots tend to emerge at lower altitudes, with the last spots of a cycle appearing at around 10° . The behaviour of sunspots during the cycle is best illustrated in the so called “butterfly diagrams” shown in Fig. 1.1.

The data displayed in Fig. 1.1 was collected in Greenwich starting in 1874 and since 1976 in Debrecen in Hungary. The maxima of the cycles are indeed separated by roughly 11 years, though the end and beginning of individual cycles overlap, i.e., low-latitude spots of the old cycle are present at the same time as high-latitude spots of the new cycle. The cycles are numbered with the cycle from 1755–1766 designated as “Cycle 1” by convention. As illustrated in the bottom of Fig. 1.1, the fraction of the area covered by sunspots is not the same for every cycle. The 19th cycle shows the maximum of sunspot coverage. One of the most drastic variations in solar activity is described by Gustav Spörer in 1889. He researched sunspot records and noted, that in the late 17th century nearly no sunspots were spotted. This event was also noticed later by Edward Walter Maunder. He states that for a period of 70 years, ending in 1716, a remarkable interruption of the ordinary course of sunspot cycles appeared, with several years without any spots (Maunder, 1890). This period of minimum activity is now called the Maunder Minimum.

Having a closer look at the magnetic polarities of sunspots, it is evident that a whole magnetic solar cycle actually lasts for 22 years. The magnetic configuration of sunspotgroups follows the Hale-Nicholson law (Hale and Nicholson, 1925), saying that in each hemisphere bipolar groups have the same magnetic orientation of leading and following spots, though the orientation is opposite in the two hemispheres. If in the northern hemisphere the pairs of spots are N-S orientated, the ones on the southern hemisphere have a S-N orientation. After an 11-year cycle, the orientation of bipolar groups reverses (Stix, 2002). According to Joy’s law, the leading spot of bipolar groups is closer to the equator than the trailing one. The inclination angle varies from a few degrees for regions near to the equator up to 15° for groups at latitudes of 35° (Hale *et al.*, 1919).

1.1.4 Structure of Umbra and Penumbra

Having a closer look at the umbra, it is evident, that it is not only dark, but contains different structures, i.e., bright features above a dark background. Even the dark background varies and the darkest parts are called dark nuclei, which occupy 10–20% of the umbra. Their intensity range between 5–33% of the quiet-Sun’s value, usual nuclei intensities are about 15% (Sobotka, Bonet, and Vazquez, 1993; Sobotka and Hanslmeier, 2005). The size of the dark nuclei is about 1000 km and therefore comparable to that of photospheric granules.

The first of two types of bright features in the umbra are umbral dots. They contribute to 10–20% of the total brightness of the umbra, while only covering 3–10% of the umbral area (Sobotka, Bonet,

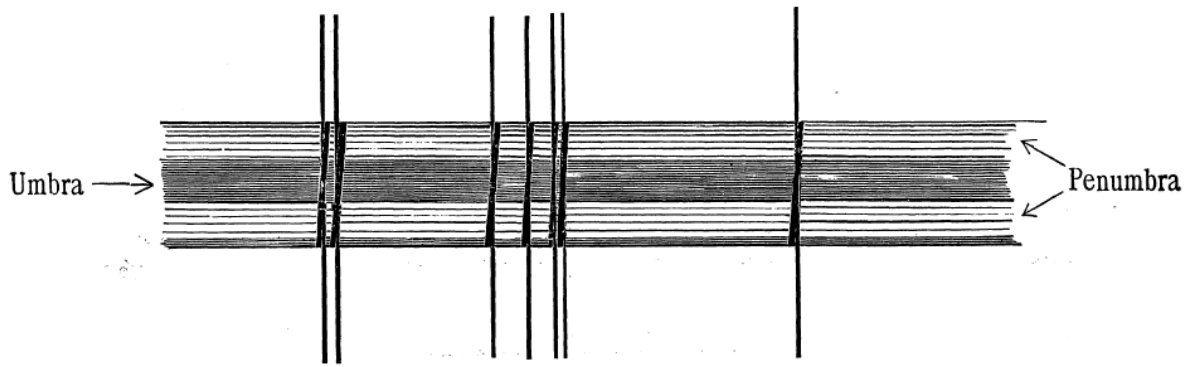


Figure 1.3: Original sketch by Evershed showing the wavelength shift of photospheric absorption lines in a sunspot penumbra (Evershed, 1909b).

and Vazquez, 1993). On average they are 500–1000 K cooler than the quiet photosphere, but 1000 K hotter than the umbra and therefore appear as bright dots (Sobotka and Hanslmeier, 2005; Kitai *et al.*, 2007). The distribution of effective diameters of umbral dots have been measured to peak at around 175 km (Sobotka and Hanslmeier, 2005). Umbral dots have an average lifetime of 14 min, but large and bright dots might last longer than two hours (Sobotka, Brandt, and Simon, 1997). The dots originate from magnetoconvection and can be interpreted as hot convective plumes that decelerate as they rise. As they expand, the magnetic field is reduced (Degenhardt and Lites, 1993a,b). The second bright feature observed in umbrae are light-bridges. They might extend all the way across the umbra, some segmented with bright and dark lanes (Berger and Berdyugina, 2003). Light-bridges appear and disappear during the lifetime of a sunspot, but the appearance of new light-bridges and brightening of existing ones are indicators of an imminent breakup of the spot (Vazquez, 1973).

The penumbra appears as a brighter region around the umbra and is still about 500 K cooler than the quiet-Sun. Observations with spatial resolutions of 1–2'' show alternating bright and dark elongated filaments with radial alignment. Some originate from the border of the umbra and penumbra, others from within the penumbra, and they may extend for 3500–7000 km. Although a spatial resolution of 1'' is able to show filaments, the width of the narrowest filaments is expected to be below 80 km (Roupe van der Voort *et al.*, 2004). At resolutions below 1'' the bright filaments are seen to consist of bright features called penumbral grains (Muller, 1973). The intensities of the brightest grains even exceed the brightest granules outside sunspots and have a higher temperature by about 150 K (Tritschler and Schmidt, 2002). Penumbral grains in the inner penumbra move inwards during their lifetime of roughly one hour and become peripheral umbral dots as they reach the umbra (Foukal, 2013). In the outer penumbra, they move outwards and often disappear before even reaching the outer penumbral boundary (Márquez, Sánchez Almeida, and Bonet, 2006).

1.1.5 Wilson Depression

In 1769 Alexander Wilson first described an effect now called Wilson depression (Wilson, 1769). As a sunspot begins to reach the limb of the Sun, the width of the disc-side penumbra decreases faster than the penumbra at the limbward side. For this reason the limb-side penumbra seems to become broader. This depression happens due to the decreased opacity of the sunspot atmosphere. The reduced temperature in sunspots causes a decrease in the H^- bound-free opacity and the lower gas pressure further reduces the opacity. As a result the sunspot appears more transparent as the surrounding quiet photosphere, allowing a deeper look into it. The Wilson depression is defined by the geometrical depth z_W which is a function of the optical depth and position within the spot. The depth was found to vary between 50–100 km in the penumbra and between 400–500 km in the umbra with a sharp transition at the border between those two (Solanki, Walther, and Livingston, 1993).

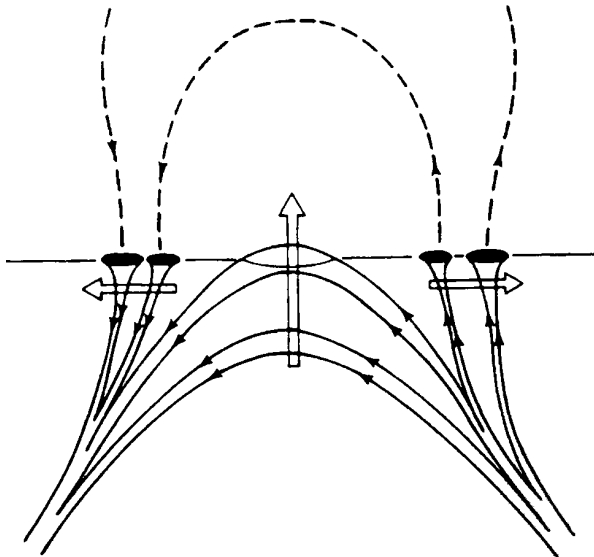


Figure 1.4: An Ω -shaped loop rises through the photosphere and leads to the formation of an active region. Flux bundles form the footpoints of the loop, the arrows indicate their local displacement (Zwaan, 1992).

1.1.6 Evershed Flow

In 1909 John Evershed discovered that sunspots are not static. He observed an outflow of plasma in the penumbra, which now is called Evershed flow (Evershed, 1909a). Evershed found displacements of spectral lines towards the blue in the center-side penumbra and towards the red in the limb-side one. The displacements varied depending on the slit position, being maximal along a line from the spot center to the center of the solar disc and being minimal perpendicular to this line. In conclusion he stated that the displacements are due to a Doppler effect caused by radial outflow from the sunspot center. The flow accelerates towards the penumbra with flow speeds of about 1 km s^{-1} at the edge of the umbra and about 2 km s^{-1} in the middle penumbra (Kinman, 1952). At the outer edge of the penumbra the flow ceases abruptly. St. John found in 1913 that the displacement of the spectral lines depends on the line strength, becoming even negative in the strongest ones and then being called the inverse Evershed effect (St. John, 1913). Due to the inversion of the effect, the flow has to be inward in the chromosphere, where the stronger lines originate.

1.1.7 Growth of an Active Region

To understand how a sunspot forms, the Sun's magnetic field and its rotation need to be investigated more closely. While the core and radiation zone of the Sun rotate rigidly, the convective zone rotates differentially. The angular rotation speed varies with the distance from the Sun's core. Furthermore, there is a large decrease of angular rotation rate with increasing latitude. While the poles make one rotation every 35 days, the equator needs only 25 days (Zirker, 2002).

Active regions develop because of magnetic flux emergence. They are formed within a few days by emerging and expanding magnetic bipoles (Zirin, 1972). A bundle of toroidal magnetic flux rises from the convection zone and finally breaks through the photosphere in fragmented form as shown in Fig. 1.4. As the bundle breaks through the surface, it is shredded into strands which are quickly concentrated into magnetic flux bundles, which might coalesce to first form pores (Leka and Skumanich, 1998). Coalescence of pores and magnetic flux tubes leads to a growing pore. As the pore increases in size and total magnetic flux, it might develop a penumbra turning it into a sunspot. The formation of the penumbra, as well as the magnetic field configuration and Evershed flow, occurs within about 20 min (Leka and Skumanich, 1998; Yang *et al.*, 2003).

The formation of an active region does not stop at the emergence of a single sunspot. Typically an active region consists of a bipolar group with several pores and sunspots with lifetimes varying on time scales between hours and several months. Large differences can be seen in the lifetimes of leading and trailing spots. Usually a large sunspot forms in the western leading part of a region by coalescence of pores and smaller sunspots. These long-lived spots often consist of a dark umbral core and are nearly circular in shape surrounded by a moat (Zwaan, 1992). The moat is originating from the moat flow, which

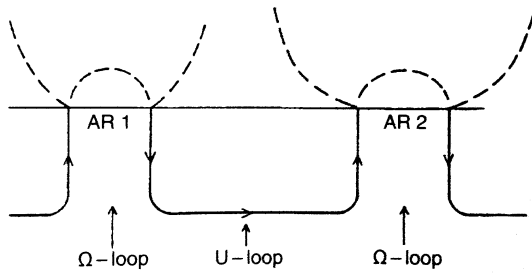


Figure 1.5: Two rising Ω -shaped loops and the formation of a U-loop in between them (Zwaan, 1992).

is at the surface a horizontal flow away from the umbra (Stix, 2002). The trailing part often consists of several irregular shaped spots and pores making up a short-lived configuration of spots. Generally, the lifetime T of a spot is proportional to its maximum area

$$A_{\max} = D_{\text{GW}}T, \quad (1.2)$$

where $D_{\text{GW}} = (10.89 \pm 0.18) \times 10^{-6} A_{\odot/2} \text{ day}^{-1}$ (Petrovay and van Driel-Gesztelyi, 1997).

1.1.8 Decay of an Active Region

As soon as all the available magnetic flux has emerged, the active region already starts to decay. Sunspots are starting to shrink and pores disappear, sometimes leaving one stable leading spot which decays slowly. The lifetime of an active region is roughly proportional to the maximum value of its total magnetic flux, with a constant of about $1 \times 10^{20} \text{ Mx day}^{-1}$ (Golub, 1980). Although, it is not unusual that a new active region rises at the same place and replaced the old one.

While the growth phase of an individual sunspot usually only lasts a few days, its decay may stretch for weeks or even months. Here, once again leading and trailing parts show different behaviours. Short-lived sunspots usually fragment rapidly, while longer-lived sunspots gradually decay (Zwaan, 1992). Gradual decay causes sunspots to shrink in size due to gradual loss of magnetic flux. The flux is redistributed from the umbra to the penumbra and finally to the surroundings until the spot or then pore ultimately fragments. The fragmentation usually starts with bright dots appearing in the umbra, which then breaks up within less than a day (Zwaan, 1968, 1987).

1.2 Spectral Lines

Studying spectral lines is elementary for reasearches of the Sun's structure. The solar spectrum contains numerous dark lines called Fraunhofer lines. They are produced by the elements composing the Sun, which absorb and emit light. The electrons of atoms can be bumped to a higher energy level by absorbing a photon, and later emit a photon when the electron falls back into its initial state (Zirker, 2002).

1.2.1 Kirchhoff's Laws

Kirchoff established three laws for spectral lines. The first one says, that a hot, dense gas or hot solid is producing a continous spectrum. This law is related to the blackbody radiation. The second law states, that a hot diffuse gas is producing emission lines. Atoms in the gas collide with each other, leading to electrons being bumped into higher energy levels. Falling back to their initial level, they emit a photon, and this is leading to emission lines with energies reffering to the energy distance of the two levels. The third law says, that a cool gas in front of a hot background producing a continous spectrum will lead to absorbtion lines. Photons from the continous spectrum will be absorbed by atoms of the gas and later emitted again, but without a favored direction. This is leading to absorbtion lines in the continous spectrum, which refer to the energy distances of allowed transitions for the electrons (Carroll and Ostlie, 2007).

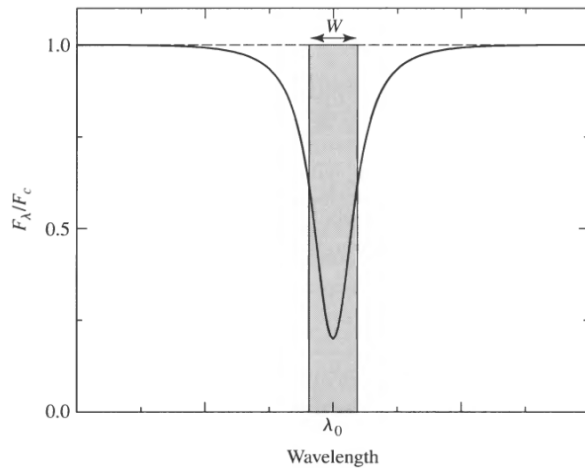


Figure 1.6: Illustration of a typical absorption line profile with the main properties. The shaded area represents the equivalent width, i.e., a rectangle with the height of unity and the same area as covered by the spectral line (Figure 9.18 in [Carroll and Ostlie, 2007](#)).

1.2.2 Profiles of Spectral Lines

Investigations of the shape of a spectral line profile provides information about the environment in which it was formed. An example of an absorption line profile can be seen in Fig. 1.6. The profile can be divided into three regions, (1) the line core, which is the region around the central wavelength λ_0 , (2) the wings, which are the sides connecting the line core to (3) the continuum. Interesting parameters of the profiles are the already mentioned central wavelength, also referred to as line core position, the amplitude, the full-width-at-half-maximum (FWHM) and the equivalent width. These properties will be important for fitting theoretical models to the line profiles as will be done in Sect. 4.2.1. As the name is implying, the FWHM is the change in wavelength of the spectral line at the positions where the intensity of the line reaches half of the intensity at the line core. To describe the strength of a line, the equivalent width is commonly used. It is defined as the width of a box centered at the central wavelength and reaching up to the continuum, which then covers the same area as the spectral line ([Carroll and Ostlie, 2007](#)).

The shape of line profiles are influenced by broadening mechanisms. First, there is the natural broadening, which originates from the Heisenberg uncertainty principle. The lines are formed by transitions of electrons between discretely spaced energy levels, which do not have a precise values due to the uncertainty principle. Therefore, the energy difference is blurred, leading to a broadening of the observed line. The second mechanism is Doppler broadening. Since the atoms in a gas are moving, the emitted and absorbed photons are Doppler shifted randomly according to the velocity of the moving atom. Doppler broadening results in roughly 1000 times greater broadening than the natural broadening. The third process is pressure and collisional broadening. Collisions with neutral atoms or being near the electric field of an ion can interfere with the electrons orbitals, and therefore leading to blurred energies of transitions between them. The magnitude of pressure and collisional broadening is comparable to the natural broadening ([Carroll and Ostlie, 2007](#)).

The line profiles are described by the so called Voigt profile, which combines two effects shaping the line profile. As mentioned, the lines are Doppler broadened and this effect is dominating the line core, but decreasing exponentially with line depth. Therefore, the Doppler profile is not describing the wings of a line profile, while a damping profile is fitting them. The mathematical formula describing the Voigt profile can also be found in Sect. 4.2.1, since it was used as a model for fitting the line profiles ([Carroll and Ostlie, 2007](#)).

1.3 Polarimetry

1.3.1 Zeeman Splitting

The presence of a magnetic field causes Zeeman splitting of spectral lines. This was what lead George Ellery Hale in 1908 to discover the magnetic field in sunspots ([Hale, 1908](#)). The splitting and the polarization of Zeeman components can be used to gain information about the magnetic field. In case of a weak magnetic field, in the sense that Russell-Saunders-coupling (LS -coupling) is an appropriate de-

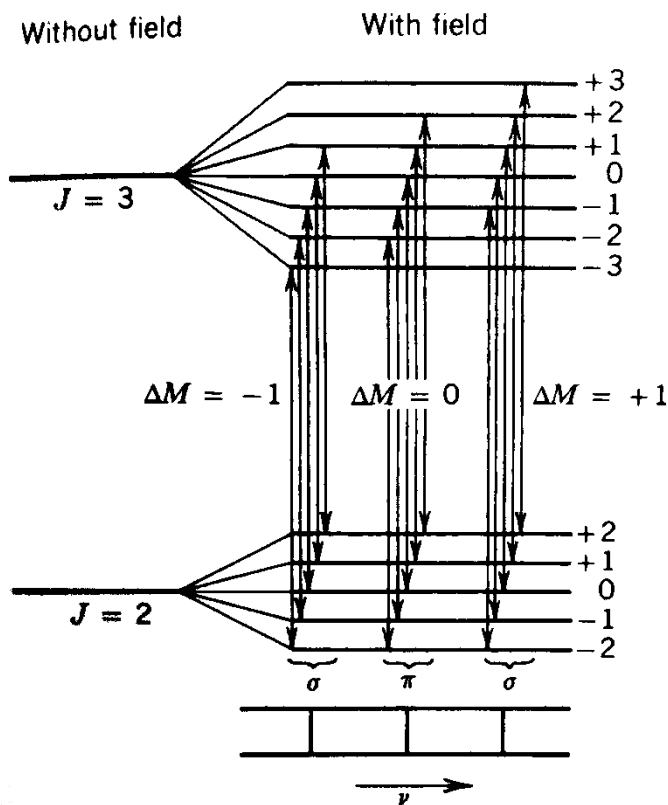


Figure 1.7: Illustration of the normal Zeeman effect for a transition between $J = 2$ and $J = 3$. Each group of arrows contributes to one line, leading to the three lines shown at the bottom (Figure 3.11 in Foukal, 2013).

scription, the state of an atom is described by the quantum numbers L, S, J , and M_J . M_J is the “magnetic” quantum number determining the component of angular momentum in the direction of the magnetic field. Without an external magnetic field all states of M_J have the same energy and are not distinguishable.

As soon as an external magnetic field is present, an energy shift occurs for the states with $M_J \neq 0$. The general case of splitting is called “anomalous Zeeman effect”. Transitions between two states of an atom are allowed if the selection rule $\Delta M_J = -1, 0, 1$ applies. Since the energy levels of the states are shifted, the spectral lines getting emitted or absorbed by the transitions split. The lines are distinguished between σ^\pm and π components depending on the value of ΔM_J , as illustrated in Fig. 1.7 (Foukal, 2013).

A special case of splitting is called “normal Zeeman effect”, and it leads to a triplet of lines. Here, the transitions occur between states with $S = 0$, which leads to equidistant energy levels for both states. All transitions with the same value of ΔM_J have an equal distance of energy levels resulting in only three distinguishable lines. The π component is unshifted with the energy of the original spectral line. (Stix, 2002).

Depending on the observer’s LOS, the components are seen differently. The “longitudinal” Zeeman effect can be observed when the LOS is along the magnetic field. Here, the two σ -components appear as circular polarized in opposite sense, while the π -component cannot be seen. If the LOS is perpendicular to the magnetic field, the “transverse Zeeman effect” occurs, and all three components can be seen. All components are linearly polarized with the π -component perpendicular and the σ -components parallel to the magnetic field vector in case of absorption. If emission occurs, “perpendicular” and “parallel” are switched and the circular polarized components of the longitudinal effect have reversed polarizations. Depending on the field strength the σ -components might overlap, but still can be resolved by taking advantage of their opposite polarization. Measurements of the longitudinal magnetic field were the basis for magnetographs.

1.3.2 Polarized Light

Later, in the 19th century, polarimeters were developed, which are able to measure the full polarization state of a spectral line as Stokes parameters (Thomas and Weiss, 2008). The Stokes parameters were introduced in 1852 by George Gabriel Stokes and are defined as follows. Considering a monochromatic,

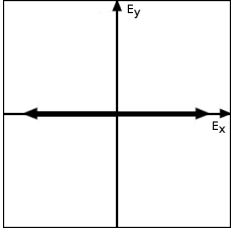
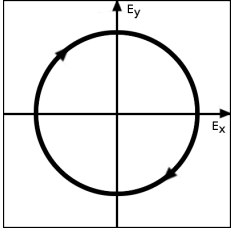
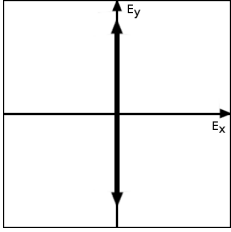
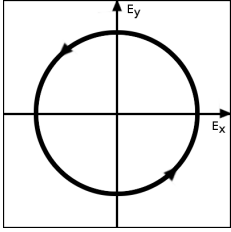
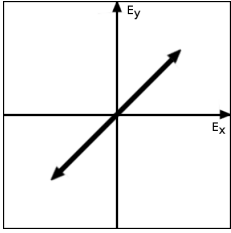
Notation	Polarization	Stokes Vektor	Notation	Polarization	Stokes Vektor
linear, horizontal		$\begin{pmatrix} 1 \\ 1 \\ 0 \\ 0 \end{pmatrix}$	circular, right-hand		$\begin{pmatrix} 1 \\ 0 \\ 0 \\ -1 \end{pmatrix}$
linear, vertical		$\begin{pmatrix} 1 \\ -1 \\ 0 \\ 0 \end{pmatrix}$	circular, left-hand		$\begin{pmatrix} 1 \\ 0 \\ 0 \\ 1 \end{pmatrix}$
linear, +45°		$\begin{pmatrix} 1 \\ 0 \\ 1 \\ 0 \end{pmatrix}$	unpolarized		$\begin{pmatrix} 1 \\ 0 \\ 0 \\ 0 \end{pmatrix}$

Table 1.1: Stokes vector for different states of polarization.

completely polarized light wave propagating in the z -direction,

$$E_x = \xi_x \cos \phi, \quad E_y = \xi_y \cos(\phi + \varepsilon), \quad (1.3)$$

define the electric field parameters, where $\phi = \omega t - kz$ and ε is the phase difference between E_x and E_y . The state of polarization is described by the constant amplitudes ξ_x and ξ_y and the phase difference. The Stokes vector is defined as

$$\vec{S} = (I, Q, U, V) \quad (1.4)$$

containing the following Stokes parameters

$$\begin{aligned} I &= \xi_x^2 + \xi_y^2, & Q &= \xi_x^2 - \xi_y^2, \\ U &= 2\xi_x\xi_y \cos \varepsilon, & V &= 2\xi_x\xi_y \sin \varepsilon. \end{aligned} \quad (1.5)$$

The parameters in Eqn. 1.5 obey the rule

$$I^2 = Q^2 + U^2 + V^2, \quad (1.6)$$

which characterizes complete polarization. In solar spectral lines the Stokes parameters are functions of the wavelength λ , because the radiation has a certain state of polarization at each wavelength (Stix, 2002). Examples for Stokes vectors for different states of polarization can be seen in Table 1.1 and a small part of a Stokes-V profile is depicted in Fig. 4.1.

Chapter 2

Instruments

2.1 Solar Dynamics Observatory

The Solar Dynamics Observatory (SDO) is a space weather mission and part of the National Aeronautics and Space Administration's (NASA's) Living With a Star (LWS) program (Pesnell, Thompson, and Chamberlin, 2012). Its purpose is to investigate the variable Sun and its impact on life on Earth. It was launched on 2010 11 February from the Kennedy Space Center and contains three instruments: the Atmospheric Imaging Assembly (AIA), the Extreme Ultraviolet Variability Experiment (EVE), and Helioseismic and Magnetic Imager (HMI). EVE observes the EUV from 0.1 – 105 nm as well as from 121.6 nm to investigate solar EUV irradiance on time scales from seconds to years (Woods *et al.*, 2012). This thesis contains data from AIA and HMI, and therefore both instruments will be described in more detail.

Science data is returned by SDO since 2010 May 1, and the space mission delivers approximately 150 000 high-resolution solar full-disc images and 9000 EUV spectra, resulting in 1.5 terabyte data each day. The data are converted into images, dopplergrams, magnetograms, and spectra. The main goals of the SDO mission is to predict space weather events, such as flares and coronal mass ejections, as well as obtaining a better understanding of the formation of active regions, the generation of the magnetic field, and the field itself (Pesnell, Thompson, and Chamberlin, 2012). A whole 22-years cycle of the solar magnetism will be observed with SDO in collaboration with other space missions, such as the Solar and Heliospheric Observatory (SoHO, Domingo, Fleck, and Poland, 1995) and Hinode (Kosugi *et al.*, 2007).

2.1.1 Atmospheric Imaging Assembly

The AIA instrument is used to investigate the dynamic coronal structure, i.e., how energy is brought into the coronal field, stored, and released. It also provides information about coronal heating and irradiance, which might lead to impacts on communications systems on the Earth and low-Earth orbit spacecrafts. The instrument consists of four Cassegrain telescopes with 20-cm primary mirrors and an active secondary mirror. All telescopes have a filter wheel to choose between different wavelength channels, and the mirrors have a multilayered coatings used to optimize them for the specific wavelengths. In addition to the mirror coatings, interference filters and coatings on the entrance windows are used for wavelength filtering (Lemen *et al.*, 2012).

Three of the telescopes have two different EUV band passes, while one telescope has one band pass in the EUV on one half of the mirror and a broad-band UV coating on the other. Telescope number one has a λ 131.0 Å band pass focusing on the transition region and flaring corona and a λ 335.4 Å band pass for the active region corona. Telescope number two has a λ 193.5 Å band pass for investigations in the corona and hot flare plasma and a λ 211.3 Å band pass once again for the active region corona. Telescope number three is the one with four band passes: λ 171.1 Å for the quiet corona and the upper transition region, λ 1600 Å for the transition region and the upper photosphere, λ 1700 Å focusing on the temperature minimum and the photosphere, and λ 4500 Å representing the photosphere. Telescope number four has a λ 93.9 Å band pass for the flaring corona and a λ 303.8 Å band pass for the chromosphere and the transition region (Lemen *et al.*, 2012).

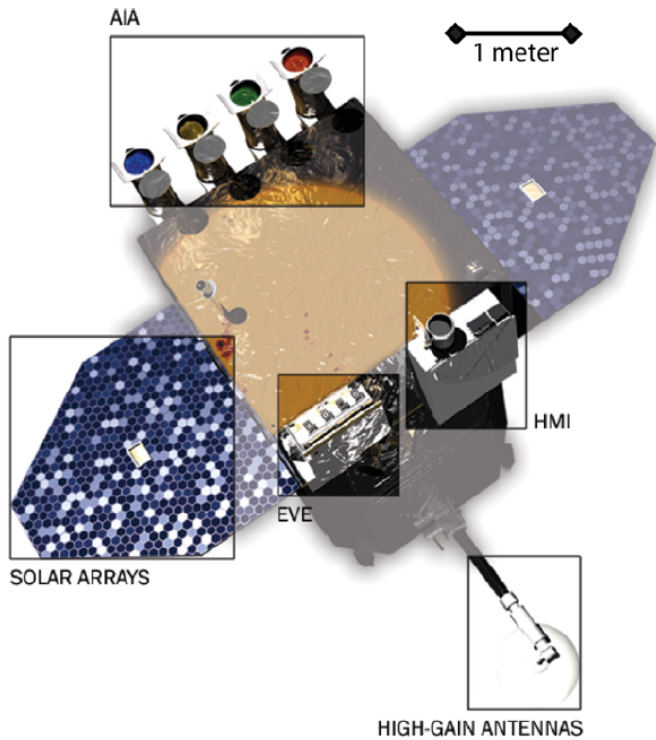


Figure 2.1: Overview of SDO showing its main instruments: AIA, EVE, and HMI. Also shown are the high-gain antennas and the 6.6 m² solar arrays, which produce 1500 W of power (Fig. 1 in [Pesnell, Thompson, and Chamberlin, 2012](#)).

Each telescope takes full-disc images containing 4096×4096 pixels with a circular field-of-view (FOV) with approximately 41' diameter. The corners of the Charge-coupled devices (CCDs) are shaded by the filter wheel and are used to monitor noise levels and energetic particles. The AIA images have a spatial resolution of 1.5'' and an image scale of $0.6'' \text{ pixel}^{-1}$ ([Lemen *et al.*, 2012](#)).

2.1.2 Helioseismic and Magnetic Imager

The HMI instrument is based on the Michelson Doppler Imager (MDI, [Scherrer *et al.*, 1995](#)) with modifications allowing higher resolution and cadence and containing a second camera. It uses the 6173 Å Fe I absorption line to measure the Doppler shift, the intensity, the LOS magnetic field, and the vector magnetic field in the solar photosphere. The scientific goals are to investigate dynamics of the convection zone and the solar dynamo, as well as the origin and evolution of active regions. Using helioseismology, like seismology on the Earth, HMI measures motions of the photosphere to provide information about solar oscillations, as well as the polarization in a spectral line to investigate all components of the photospheric magnetic field ([Schou *et al.*, 2012](#)).

The instruments contains two CCDs with 4096×4096 pixels providing images with an image scale of $0.5'' \text{ pixel}^{-1}$ and a spatial resolution of 0.9''. Full-disc images are taken every 3.75 s, leading into a cadence of 45 s for Doppler velocity, LOS magnetic flux, and continuum proxy images. Vector magnetic field maps can be taken every 90–135 s, depending on the selected image frame sequence ([Scherrer *et al.*, 2012](#)). The LOS magnetograms used later in the thesis are an additional product of the Doppler-velocity observations used for helioseismology.

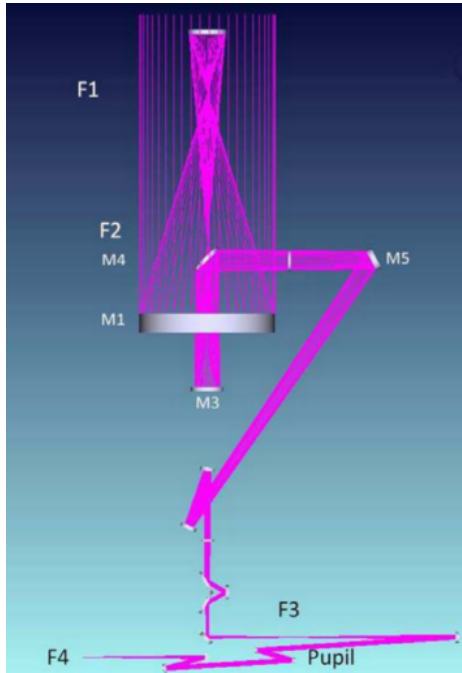


Figure 2.2: Design of the GREGOR solar telescope with the mirrors M1 to M5 and the focal planes F1 to F4 (Fig. 5 in [Schmidt et al., 2012](#)).

2.2 GREGOR Solar Telescope

GREGOR, the name hinting at the telescope being a large Gregory-type one, is one of the first new solar telescopes going beyond the 1-meter aperture limit of conventional vacuum designs. Much dynamics in the solar atmosphere occurs at scales around or even below 100 km. To allow observations at such small scales, high spatial and temporal resolution are needed, which can only be reached with large-aperture telescopes at sites with extremely good seeing ([Kneer, 2012](#)). The official proposal for the construction of the GREGOR telescope was prepared in 2000 March and after 10 years of planning and construction, the installation of GREGOR was completed around May 2011. Science verification then started in spring 2012.

GREGOR has an aperture of 1.5 m and replaces the former 45-cm Gregory-Coudé Telescope (GCT, [Kneer and Wiehr, 1989](#)). It is located in the Observatorio del Teide on the Canarian Island Tenerife and was built by the German consortium of the Kiepenheuer-Institut für Sonnenphysik (KIS), the Institut für Astrophysik Göttingen (IAG), the Leibniz-Institut für Astrophysik Potsdam (AIP), and the Max-Planck-Institut für Sonnensystemforschung (MPS). The telescope achieves a spatial resolution down to $0.1''$ which is about 70 km on the Sun ([Schmidt et al., 2012](#)). The scientific goals of GREGOR are to study and understand

- the interaction between the photospheric magnetic field and convection,
- the sunspot fine structure,
- the solar magnetism in respect to solar variability, and
- the enigmatic chromospheric heating mechanisms.

2.2.1 Telescope Design

GREGOR contains three imaging mirrors. The primary mirror M1 is paraboloid with a focal length of $f_1 = 2500$ mm and has a diameter of $D_1 = 1500$ mm. The two elliptical mirrors M2 and M3 build the double Gregory system of GREGOR. They have diameters and focal lengths of $D_2 = 400$ mm, $f_2 = 520$ mm, $D_3 = 300$ mm, and $f_3 = 1400$ mm. M2 forms a secondary image and reflects the beam to the GREGOR Polarimetric Unit (GPU, [Hofmann et al., 2012](#)), and then towards M3. The tertiary forms the final image, which is fed into the observing laboratory by further flat folding mirrors ([Schmidt et al., 2012](#)).

The telescope has an effective focal length of $f_{\text{eff}} = 58\,950$ mm. This leads to the focal ratio of $f/D \approx 39$ and an image scale of $3.5'' \text{ mm}^{-1}$. A circular FOV with a diameter of $180''$ can be observed. This limit results from the heat stop; the theoretically diameter of the FOV is $300''$ ([Denker et al., 2012](#)).

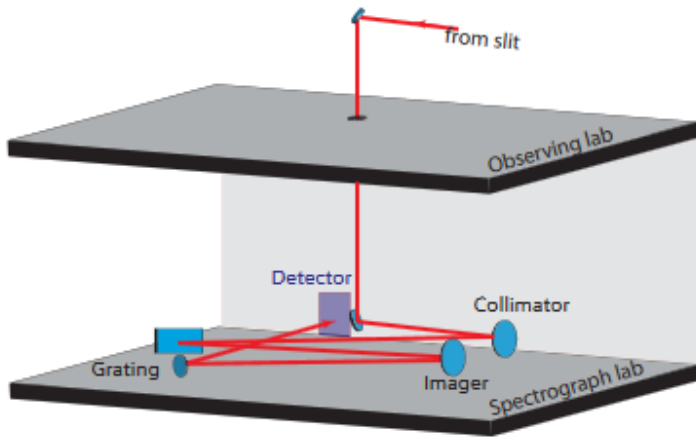


Figure 2.3: Schematic drawing of GRIS. Light enters the spectrograph laboratory from above through an opening in the floor. It gets reflected to the collimator with a folding mirror and then travels to the grating before being finally reflected by the camera mirror to the detector (Fig. 10 in [Schmidt et al., 2012](#)).

2.2.2 GREGOR Infrared Spectrograph

The GREGOR Infrared Spectrograph (GRIS) inherited many features of the already existing instrument at the Vacuum Tower Telescope (VTT). GRIS uses a Rockwell TCM 8600 infrared 1024×1024 pixel detector of the Tenerife Infrared Polarimeter-II (TIP-II, [Collados et al., 2007](#)). The sensor acquires data at a maximum frame rate of 30 Hz with a square pixel size of $18 \mu\text{m}$. The grating of the old GCT is also reused, providing a grating constant of $316 \text{ lines mm}^{-1}$ and a blaze angle of 63.4° at dimensions of 370 mm (width) and 190 mm (height).

GRIS covers a wavelength range between 1000–2200 nm. The angular resolution of GREGOR at the two most used spectral regions at $1.083 \mu\text{m}$ (He I triplet and a Si I line) and at $1.565 \mu\text{m}$ (a Fe I line with $g = 3$) is $0.18''$ and $0.26''$, respectively. Therefore a sampling of $0.18''$ is used.

The optical path can be seen in Fig. 2.3. The entrance slit has a length of 50 mm ($180''$) and a width $70 \mu\text{m}$ ($0.25''$). A slit-jaw imaging system with three channels allows to record images in different wavelengths, using the FOV not covered by the spectrograph slit. The first channel is used to record broad-band continuum images above 656 nm. For chromospheric imaging at 656.3 nm ($H\alpha$), the second channel is used, while the third one remains unused for the moment ([Collados et al., 2012](#)).

2.2.3 Polarimeter

For spectropolarimetric measurements, TIP-II is used. It is located directly after the slit and consists of a pair of ferroelectric crystals (FLCs) to modulate the polarization information and a polarizing beam-splitter. The FLCs have a fixed retardance and an optical axis, that alternates between two orientations controlled by application of an external voltage. The angle between the two orientations is temperature dependent, and in the range of $25\text{--}30^\circ\text{C}$ it is roughly 45° . The usage of two crystals leads to four different combinations of axis orientations and allows all four Stokes parameters to be measured almost simultaneously ([Mártinez Pillet et al., 1999](#)). After the FLCs, a beamsplitter, composed of five cubes, comes to use. The beamsplitter produces a double image of the slit, with the two images being aligned and linearly polarized at $\pm 45^\circ$. The cubes are arranged in a way, that both images travel the same optical path length, but they are separated by 28.2 mm. This separation is reduced to 18 mm by a system of prisms. In its polarimetric mode the slit length is reduced to 18 mm ($65''$). The detector is located outside the spectrograph room to simplify access to the liquid-nitrogen cooled dewar ([Collados et al., 2012](#)).

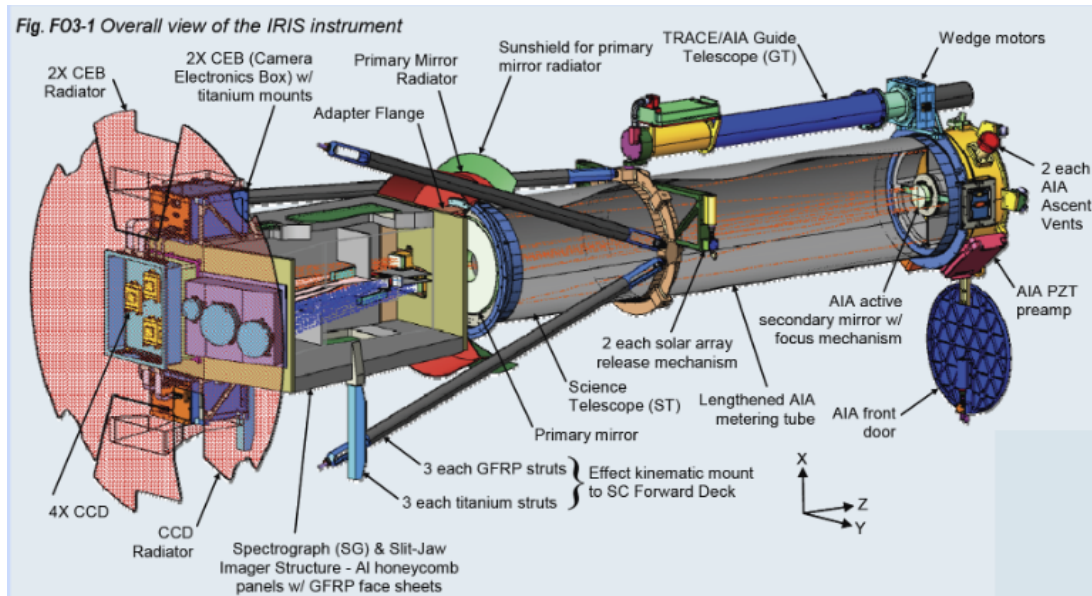


Figure 2.4: Overview of the IRIS instrument. Light enters the telescope from the right and is guided towards the spectrograph and the slit-jaw imager (Fig. 8 in [de Pontieu et al., 2014](#)).

2.3 Interface Region Imaging Spectrograph (IRIS)

2.3.1 Overview and Mission Details

The Interface Region Spectrograph (IRIS, [de Pontieu et al., 2014](#)) was launched on 2013 June 27. The satellite is in a low-Earth, Sun-synchronous orbit. This allows about eight months of eclipse-free observations. IRIS obtains spectra and images from the photosphere up to the corona, focusing on the so-called interface region between these two. The interface region is formed by the chromosphere and the transition zone, and here most of the non-radiative energy of the Sun is converted into heat and radiation. IRIS investigations focus on three themes regarding the following questions.

- Which non-thermal energy types dominate / prevail in the chromosphere?
- How does the chromosphere contribute to energy and mass supply to corona and heliosphere?
- How do magnetic flux and matter advance through the atmosphere, and how does flux emergence contribute to mass ejections and flares?

Observations coordinated with Hinode ([Kosugi et al., 2007](#)), SDO, and ground-based observatories are a high priority.

2.3.2 Telescope

The instruments are mostly based on designs of the Transition Region and Coronal Explorer (TRACE, [Handy et al., 1999](#)), AIA, and HMI. IRIS contains a 19-cm Cassegrain telescope, which means, it has a concave primary and a convex secondary mirror. The light entering the telescope reaches the primary mirror, and the UV light is reflected to the secondary mirror, while most of the visible and infrared light passes through. The secondary mirror focuses the light on the spectrograph slit. Figure 2.4 shows an overview of this set-up. More detailed information about the telescope is given in [Podgorski et al. \(2012\)](#).

2.3.3 Spectrograph and Slit-Jaw Imager

The slit assembly of the spectrograph is a prism with a reflective coating, also containing the slit, which is 0.33'' wide and 175'' long. The coating reflects light into the slit-jaw imager path, while the light going through the spectrograph slit into the prism is dispersed. Light with wavelengths in the far ultraviolet (FUV, 1332 – 1407 Å) and in the near ultraviolet (NUV, 2783 – 2835 Å) are directed onto separate parts

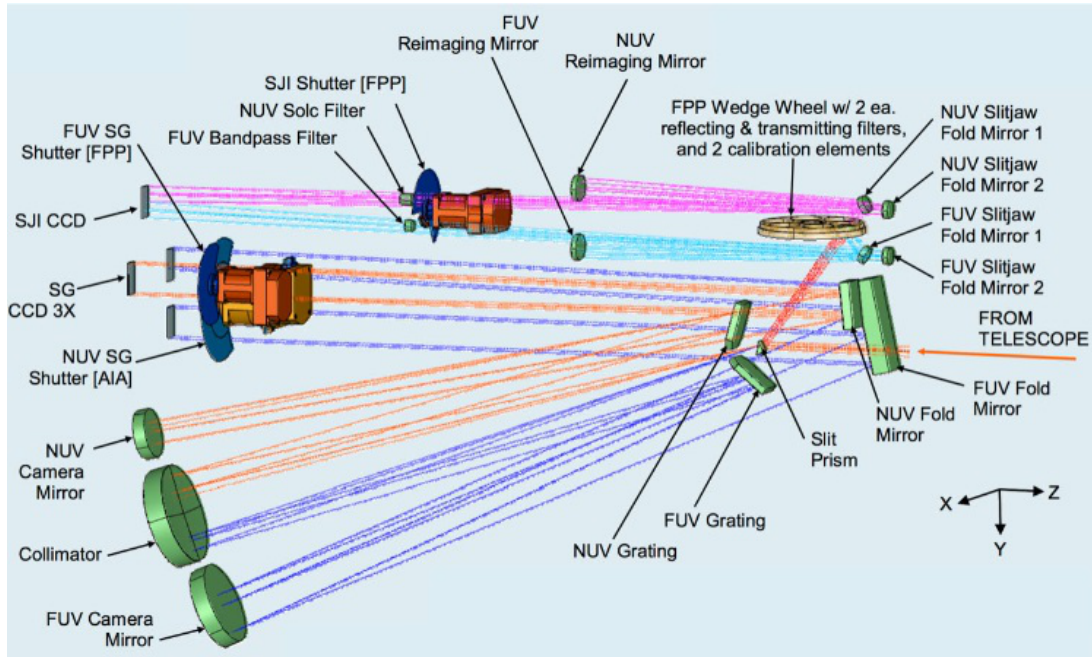


Figure 2.5: Inside the spectrograph (FUV: dark blue lines, NUV: orange lines) and the Slit-Jaw Imager (FUV: light blue lines, NUV: purple lines) the light takes various paths depending on the wavelength range (Fig. 9 in [de Pontieu et al., 2014](#)).

of the collimator mirror. This assures that both passbands image the same region of the Sun within a FOV of $0.33'' \times 175''$. The images are recorded on three different CCDs, with two CCDs for the FUV for different wavelength ranges. One includes two bright C II lines ($1332 - 1358 \text{ \AA}$), and the other one contains Si IV and O IV lines ($1389 - 1407 \text{ \AA}$).

Light reflected by the prism enters the slit-jaw imager, which contains a filter wheel. It consists of six different filters, of which only four are actually used for solar observations, while the other two are used for calibration. The FOV for slit-jaw images is $175'' \times 175''$. Filters for the NUV are transmitting, while filters for the FUV are reflective, ensuring separate paths for both. But finally both beams pass the same shutter mechanism and are recorded on different halves of the same CCD. The lightpaths inside the spectrograph and slit-jaw imager are illustrated in Fig. 2.5 ([de Pontieu et al., 2014](#)).

2.3.4 Detectors

IRIS CCDs all have 2061×1056 pixels and two readout amplifiers, enabling simultaneous read out of both CCD halves. The CCDs provide a quantum efficiency of 31% at 1400 \AA . IRIS data is read out at $2 \text{ mega pixels s}^{-1}$, with a read noise of less than 20 electrons. Each pixel of $13 \mu\text{m}$ side length corresponds to $0.167''$ in the spatial direction and 12.8 m\AA (FUV spectra) or 25.5 m\AA (NUV spectra) in the spectral direction, respectively. IRIS has an effective spatial resolution between $0.33''$ for the FUV and $0.4''$ for the NUV, and an effective spectral resolution between 26 m\AA for the FUV and 53 m\AA for the NUV ([de Pontieu et al., 2014](#)).

Chapter 3

Observations

3.1 Overview

Observations of celestial bodies from the Earth have to pass through the atmosphere, which is in turbulent motion. This leads to a varying optical refractive index along the LOS, and therefore, influences the image quality (Mullan, 2010). As a result the resolution of the telescope depends on the seeing parameter r_0 , rather than on the telescope diameter. For the observations presented here, the seeing was good to very good, with r_0 between 12 – 22 cm and stayed stable during the two scans. But even in good seeing conditions, adaptive optics systems are required to reach the diffraction limit of the 1.5-meter GREGOR telescope (Berkefeld *et al.*, 2012).

The target of the observing campaign was active region NOAA 12396. It appeared on the south-eastern limb of the solar disc on 2015 August 3 as a plage, and could be seen until August 14. During its disc passage, active region NOAA 12396 developed into a complex region with several sunspots of different sizes and pores, and it was the source of several B- and C-class flares.

On August 4, the region grew and developed the first few pores. On the next day, it already consisted of a leading sunspot with a light-bridge, while the trailing part was still forming. On August 6, the day of the GREGOR observations, the group was on the eastern limb and was still increasing in sunspot area and sunspot count. It had a bright H α plage and a weak $\beta\gamma$ magnetic configuration, leading to a classification as $\beta\gamma/\beta$. This means that active region NOAA 12396 consisted of a bipolar group, with a structure too complex to separate the polarities by just a single magnetic neutral line. By then the region contained an E-type sunspot, meaning that it consisted of a large bipolar group, which has at least two sunspots, that have a penumbra and often complex structure, as well as numerous small spots and extends longitudinal between 10° – 15° on the Sun (Stix, 2002).

The day after the observations, the region had added significantly in sunspot area while maintaining its magnetic configuration. On August 8, it had slightly decayed and on August 9, it lost its magnetically complex structure, but remained an E-type sunspot. The next day, the region had slightly grown in sunspot area, while having significantly increased in sunspot count. On August 11, the region entered its decay phase. As the region reached the western limb and vanished out of view, while the leading sunspot had not decayed yet. The observations focus on the southern part of the trailing spots of active region NOAA 12396. It consisted of three sunspots with non-uniform penumbrae and some pores with mixed polarity. As already indicated by the Hale classification, the region was bipolar with a complex magnetic neutral line.

Figure 3.1 gives an overview of the active region NOAA 12396 on August 6 at 08:38 Universal Time (UT), based on data from the SDO. The database contains images with 4096 × 4096 pixels covering the whole solar disc. We cut out those images to zoom in on NOAA 12396, showing the whole region. GREGOR observations at this time covered the region inside the rectangle, and therefore two of the trailing sunspots. The continuum image shows several sunspots and pores. The leading sunspot is nearly circular shaped as well as its penumbra, which becomes somewhat irregular at the left side. NOAA 12396's trailing part consists of three sunspots and several darker features and pores.

In the magnetogram, the leading part of the region is of positive polarity and has a tail that invades into the negative polarity of the trailing part. The GREGOR FOV covers a magnetic field with negative

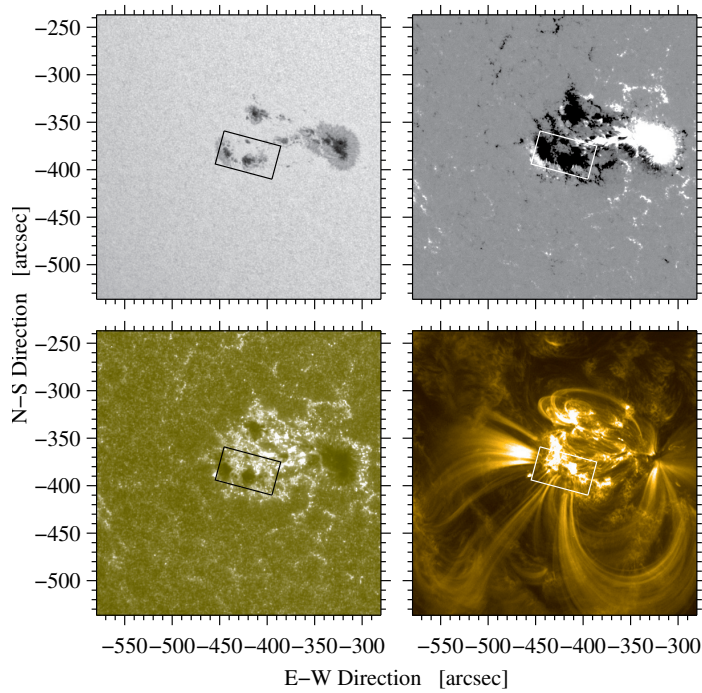


Figure 3.1: Overview of the active region NOAA12396 on 2015 August 6 at 08:38 UT. HMI continuum image (top-left), HMI magnetogram (top-right), AIA $\lambda 160$ nm image (bottom-left), and AIA Fe IV $\lambda 17.1$ nm image (bottom-right). The rectangle is outlining the FOV covered by the GREGOR observation.

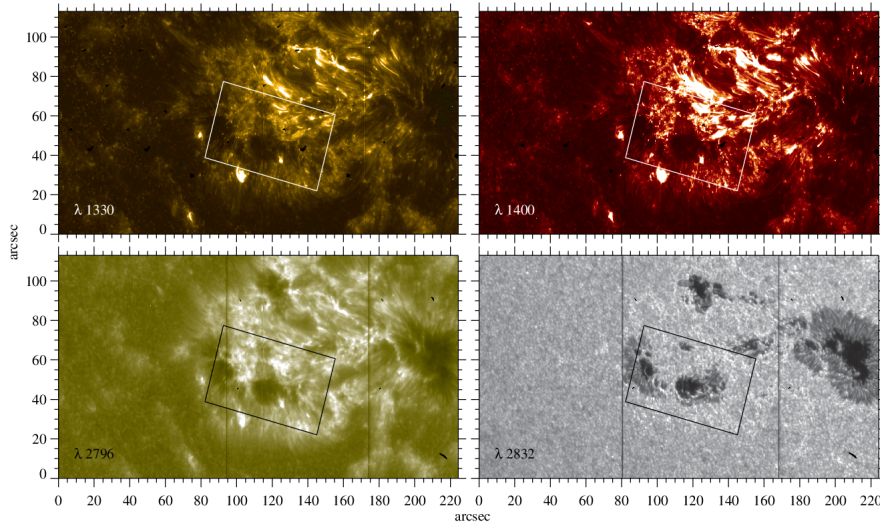


Figure 3.2: Collage of IRIS slit-jaw images in spectral lines 133 nm (top left), 140 nm (top right), 279.6 nm (bottom left), and 283.2 nm (bottom right) covering the entire active region NOAA 12396 observed on 2015 August 6 at 06:30 UT. The rectangle is outlining the FOV covered by the GREGOR observations.

polarity and lies on the edge of the magnetic neutral line. The AIA $\lambda 160$ nm image shows NOAA 12396 in the chromosphere. Bright features, so called plages, can be seen. Plages represent the same magnetic structures as faculae, which can be seen in the photosphere, but at different heights (Thomas and Weiss, 2008). They show up wherever magnetic activity is present, as can be seen when comparing the image to the magnetogram. The lower-left panel of Fig. 3.1, an AIA Fe IV $\lambda 17.1$ nm image depicts structures in the corona. Bright magnetic loops span between regions of opposite polarities. Some loops connect places within the trailing part itself, others stretch from the trailing spots to the leading one.

IRIS high-resolution slit-jaw images provide unprecedented details of the Sun’s interface region and are used to complement the SDO data. Here, level 2 images after basic calibration are presented, i.e., dark and flat-field calibration. IRIS observations were not simultaneously with GREGOR observations, however, there are data available from a few hours earlier. On 2015 August 6, the IRIS spectrograph was running large, coarse 64-step raster observations from 06:19–06:37 UT. The images were captured in the C II 133 nm, Si IV 140 nm, and Mg II k 279.6 nm channels as well as in the continuum at 283.2 nm. The data contain 16 images per channel and were recorded with a cadence of 68 s. Figure 3.2 shows 16 images fitted together, each with a FOV of $119'' \times 119''$. Since there is no time-sequence with IRIS, only a snapshot is presented, showing the region before the GREGOR observations. IRIS images cover the entire active region in the FOV.

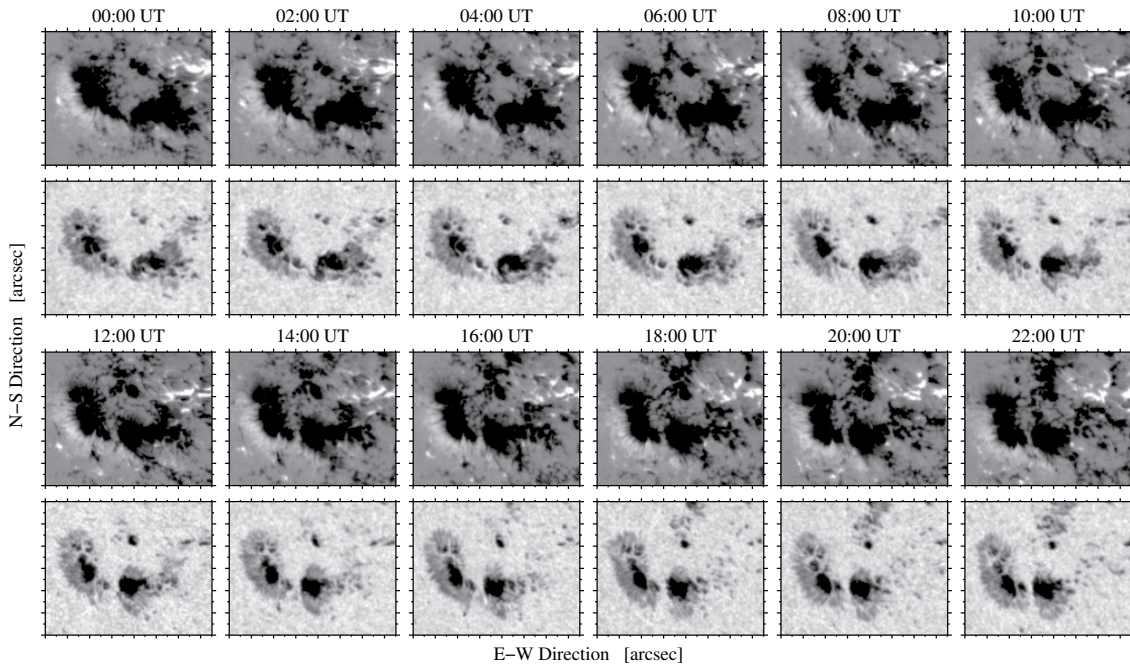


Figure 3.3: Regions-of-interest (ROI) selected from HMI magnetograms and continuum images ($75'' \times 60''$) show sunspots of the trailing part of the active region NOAA 12396, which was also observed with GREGOR. The image series shows the temporal evolution of the spots centered at the time of the GREGOR observation between 08:38–09:34 UT at two-hour intervals. The magnetograms are displayed between ± 250 G.

The continuum image at $\lambda 283.2$ nm contains the leading sunspot with a light-bridge along with three sunspots in the trailing part. In the region between trailing and leading sunspots many mixed-polarity pores are present. Brightenings are visible at this location in all the other images. In addition, many small brightenings located at the edges of trailing sunspots are seen, e.g., at coordinates ($100''$, $35''$) and ($80''$, $50''$). A visual inspection reveals that brightenings in the IRIS $\lambda 279.6$ nm image match the brightenings in the SDO/AIA $\lambda 160$ nm image (see Fig. 3.1). Furthermore, filamentary structures extending beyond the photometric boundary of the sunspot penumbra are present around the sunspots.

3.2 Temporal Evolution

3.2.1 Photometric and Magnetic Evolution

To see the temporal evolution of the active region before and after GREGOR observations, one continuum image and one magnetogram from the SDO/HMI database are chosen every two hours for the whole day, starting at 00:00 UT and ending at 22:00 UT. A ROI was selected from the full-disc data, resulting in twelve $75'' \times 60''$ images shown in Fig. 3.3. Since the region is crossing the solar disc and the Sun is rotating differentially, the images were aligned. Therefore, a standard model for solar rotation was used to map all images to the reference image observed at 12:00 UT. The continuum images are also corrected for the center-to-limb variation in intensity.

In the continuum images two sunspots are present, both with incomplete penumbra. The eastern (left) one is fairly stable in its shape on August 6. At 00:00 UT a light-bridge is forming in the lower part of its umbra. It is fully formed at 04:00 UT, dissolves afterwards, and can not be seen any longer after 8:00 UT. The umbra of the western (right) sunspot has an irregular shape at the start, but becomes more compact, forming a nearly circular penumbra over the course of the day. Over the day the penumbra drastically changes its shape. At first, it is mostly located at the top and right side of the spot. It is shifting more to the right side, then starting to dissolve at the side, while evolving at the top and bottom. Towards the end of the day it shrinks at the top once again, so that finally the penumbra is located at the bottom of the spot. Located above the two spots is a region which was constantly changing during the observations, with magnetograms showing ongoing flux emergence. This flux emergence is presumed to be preventing the formation of a steady penumbra, which was observed before by [Schlichenmaier et al. \(2010\)](#). Above

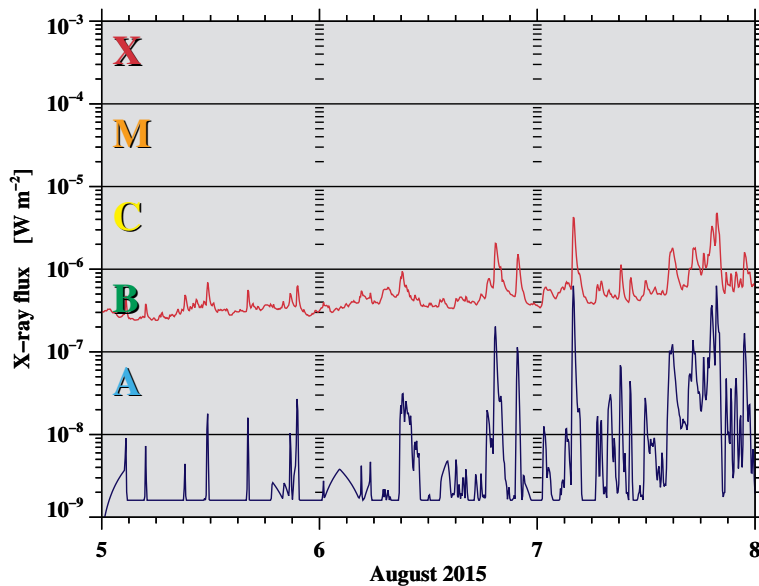


Figure 3.4: GOES 15 X-ray flux (5-minute data) covering the time period August 5–8 in the 0.1–0.8 nm (top) and 0.05–0.4 nm (bottom) energy channels.

the two sunspots in the center of the image, a pore evolves. At 00:00 UT two micro-pores appear, which were not very dark, yet. Until 6:00 UT they merged to a single pore, which grew and darkened in the following hours. After 12:00 UT it begins to shrink while new features pop up above the pore. This pore and the surrounding features later developed into a sunspot (not shown in Fig. 3.3). These observations hint towards sunspot creation by advection of smaller magnetic flux elements.

As the magnetogram shows, both sunspots are of negative polarity with traces of positive polarity at the bottom left side of the eastern spot. At the top right of first images, an intrusion of positive polarity is evident. For the time of the observations this intrusion has developed into a region of mixed polarities, and the positive polarity starts to dissolve somewhat, but it was still present in the image taken at 22:00 UT.

3.2.2 Temporal Evolution of Solar Activity

To monitor solar activity, the Geostationary Operational Environmental Satellite (GOES) measures the X-ray flux. The X-ray flux on the three days centered around the GREGOR observation is given in Fig. 3.4. Two lines represent the X-ray flux in the 0.1–0.8 nm (red) and 0.05–0.4 nm (blue) energy channels. The X-ray flux is scaled logarithmically, and the height of the 0.1–0.8 nm line can be used to determine the class of the flares. They are classified as A, B, C, M, and X-class flares, i.e., a peak flux in the order of 10^{-5} in the 0.1–0.8 nm channel corresponds to a M-class, and a flux of 10^{-6} to a C-class flare. Within the classes, a linear scale is applied, leading to, i.e., C1–C9-class flares (2016 March 30, 11:00 UT, sunearthday.nasa.gov).

Overall the solar activity was low until August 7 and once again after August 9. In between, active region NOAA 12396 was responsible for most of the solar activity on the solar disc. A list of flare events is provided by the web service solarmonitor.org. The region produced a total of 18 B-class and 19 C-class flares over a period of 13 days. On August 5, the first day of the time period shown Fig. 3.4, active region NOAA 12396 produced five B-class flares. The solar activity was still very low on that day, and it was probable that the region would only cause B-class flares. On August 6, the overall solar activity increased, although it was still considered low. During the day, the region caused three C-class flares. It was expected, that the region would be the cause of more B-class, possibly C-class flares, and with a slight chance of an isolated low-level M-class event. August 7 was the day with highest activity of active region NOAA 12396, including three B-class and eleven C-class flares. At 19:34 UT the regions highest rated event occurred, a C5.4 flare. Chances for an M-class event grew, and C-class flares were probable, but during the next day only four C-class flares occurred and the activity level began to decrease. On the following days until August 13, one more C-class flare occurred, as well as eight B-class events.

Chapter 4

Results

4.1 Basic Data Reduction and Pre-Processing

4.1.1 Basic Data Reduction

The GREGOR observations started at 08:36 UT on 2015 August 6, obtaining spectropolarimetric data in the He I 10 830 Å spectral region. It contains the photospheric Si I 10 827 Å and Ca I 10 834 Å lines, the chromospheric He I 10 830 Å triplet, and five telluric lines, which originate in Earth's atmosphere. The wavelengths were taken from the National Institute of Standards and Technology (NIST, nist.gov). The scans were carried out with 300 steps with a step size of 0.144'' leading to a scan width of 43.2''. The slit is covered by 453 pixels with a scale of 0.136'' pixel⁻¹, which leads to a 62'' scan length. The spectral range contains 1010 points with a dispersion of 1.81 mÅ pixel⁻¹. Therefore the GRIS scans cover a FOV of 62'' × 43'' and a spectral range of about 18.32 Å.

The Si I line is a strong photospheric absorption line at 10827.089 Å. It originates from the transition between the terms $4s\ ^3P_2$ and $4p\ ^3P_2$ with a Landé factor $g_{\text{eff}} = 1.5$, whereas the formation of the He I triplet occurs in the upper chromosphere (Avrett, Fontenla, and Loeser, 1994). It originates from three transitions between the lower $2s\ ^3S_1$ and upper $2p\ ^3P_{2,1,0}$ level. Although three lines belong to the triplet, only two can be observed, because two of the lines are blended (Trujillo Bueno *et al.*, 2002; González Manrique *et al.*). The two components blended lines at 10830.30 Å and 10830.25 Å are called “red” component and the unblended line at 10829.09 Å is called “blue” component. Apart from Si and He spectral lines, we have another photospheric Ca I 10839.00 Å line. The origin of Ca I resulted from the transition between $4p\ ^3P_2$ and $3d\ ^3P_2$ level. This line is also magnetic sensitive with a Landé factor $g_{\text{eff}} = 1.5$. All three magnetic sensitive lines provide information about magnetic fields and their coupling between the photosphere and chromosphere (e.g., Rüedi, Solanki, and Livingston, 1995; Kuckein, Martínez Pillet, and Centeno, 2012).

Figure 4.1 shows an overview of the information contained in the data with the Si line as an example. The upper left panel shows an image of the sunspot. It is a map, displaying the summed intensities of the whole spectrum for different positions on the Sun. A white line was added to illustrate the position of the slit for which the adjacent panels were created. The upper right panel shows the spectrum around the Si line. Here, the Zeeman splitting occurring in the sunspot umbra can be clearly seen. It is also evident in the lower left panel showing the circular polarization for the same part of the spectrum. Finally, a Stokes-V profile for a specific location is presented in the lower right panel. The two lower panels demonstrate the state of polarization of the splitted Si line. Both lines are circular polarized in opposite sense.

The basic data reduction of data is already performed on-site using the GRIS data pipeline. The various steps include dark current subtraction, flat-fielding, crosstalk removal, and calibration of polarization modulator. For flat-fielding, a quiet-Sun region near solar center was scanned with 15 scan steps and 10 accumulations while the telescope pointing was continuously changing. In addition, the calibration of polarization modulator is carried out, by calculating the polarimeter's response at the observed wavelength after generating light beams of known polarization states. This is achieved by inserting a calibration unit at an appropriate position in the beam, which contains a linear polarizer inclined at an angle and a retarder on a rotation stage. Data similar to usual scans are taken with the calibration unit in the beam path. These observations are used to compute the modulation matrix, which in turn is used for

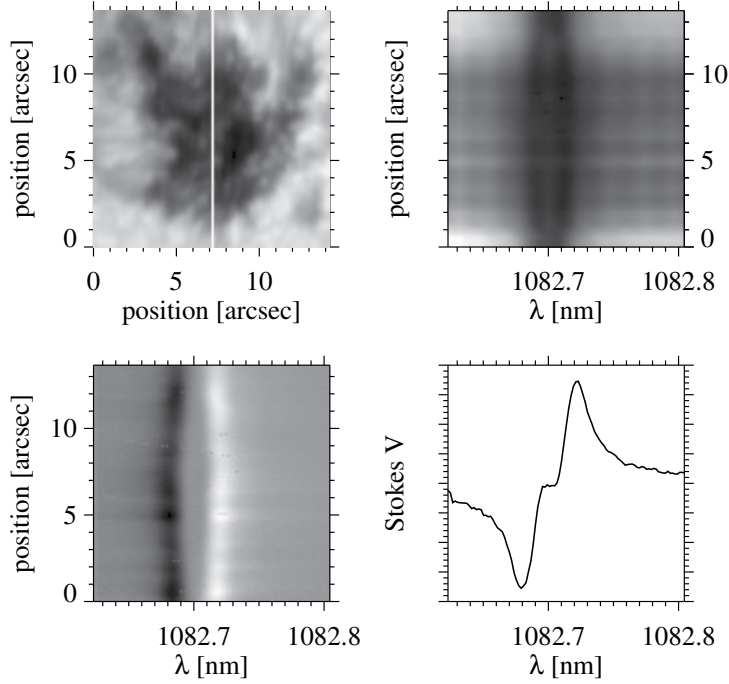


Figure 4.1: In the upper left panel an image of a sunspot is shown, where a white line indicates the slit position of the spectrum in the adjacent panel. The lower left panel shows the corresponding circular polarisation for the same spectrum. In the neighbouring panel the corresponding Stokes-V profile is shown. A splitting of the line can be seen clearly within the umbra of the sunspot. The spectral line shown here is the Si I-line at 10827.089 Å.

the calibration. The final step of the basic calibration includes removal of cross-talk. The measurement of the Stokes parameter is affected by so called “seeing-induced” crosstalk. This means that temporal variations of the parameters at scales below 0.5 s lead to false polarization signals. As described in Sect. 2.2.3, the polarimeter produces two beams, which are used to reduce this crosstalk. However, a certain amount of residual cross-talk is left in the combined beams. This is corrected using a statistical method explained in details in Schlichenmaier and Collados (2002).

A demonstration of the data after this basic corrections is shown in Fig. 4.2. There are still artefacts in the profiles which need to be dealt with. They are caused by the spectrograph instrument profile, variations in sky brightness, and the drift in the spectrograph over time. Whenever physical properties should be extracted from data, a careful preparation of the data is needed, and, therefore, the pre-processing will take an important part of this thesis. The details of the applied procedures to further correct the observed spectral profiles will be discussed in the following section.

To create both Figs. 4.1 and 4.2, as well as for further analysis, the dispersion must be calculated. The spectral information of the observed data is contained in the 1010 pixels around a central wavelength, which was 1083 nm. Therefore, this value was taken as a first guess for the actual central wavelength and 1.8 pm as initial estimate for the dispersion (Collados et al., 2012). Then, a near-infrared atlas profile (Wallace, Hinkle, and Livingston, 1993) was taken as reference, and the central wavelength as well as the dispersion were changed until the highest correlation between the atlas and the observed spectrum was achieved. The central wavelength was computed to be 10827 nm and the dispersion as 1.816 pm.

4.1.2 Pre-Processing

The pre-processing of the spectral profiles starts with creating a binary mask for the quiet Sun, i.e., only regions covered by granulation. For this an average intensity image is created, summing the intensities for all observed wavelengths. The mask was created in two steps. First pixels containing granulation were chosen, and afterwards pixels with strong helium absorption were eliminated. To detect granulation in the averaged image, an intensity threshold set at 95% of the maximum intensity was chosen, and pixels with an intensity lower than the limit are discarded. This binary mask was then further improved. Patches containing less than 2000 pixels got discarded, to avoid choosing granulations near to or containing dark magnetic features. Then, the selected patches were made bigger by morphological dilation with a 21×21 -pixel kernel. The same kernel is then used for the morphological erosion to shrink these regions.

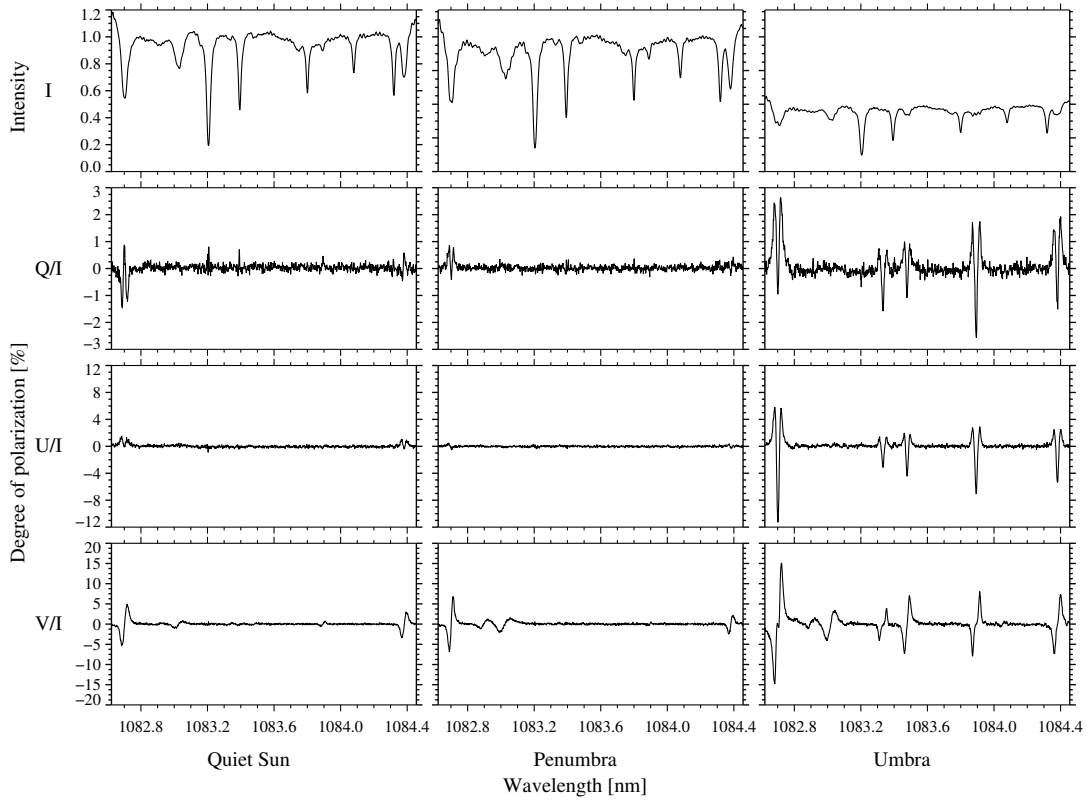


Figure 4.2: Stokes profiles from GRIS at 08:38 UT containing intensity and Stokes Q, U, and V (from top to bottom) in the quiet Sun (left), the penumbra (middle), and the umbra (right). The intensity profile was preliminarily normalized by continuum intensity of 10 000.

This two step procedure (morphological closing) cleans the mask. The mask's second propose is to avoid pixels with strong helium absorption. The presence of helium indicates magnetic structures and therefore regions with strong helium lines do not represent the quiet Sun. The helium mask is created in the same fashion as the previous mask, with the difference of using only the ± 5 wavelength points centered at the central wavelength of helium to create the initial average image. Finally both mask are combined and used to select regions containing only quiet-Sun granulation, and to compute an averaged quiet-Sun profile for further analysis.

In principle the observed spectra should exactly fit the atlas spectra. However in observed spectra there is usually a trend because of the instrument itself. To estimate the trend in the observed spectra and to afterwards correct the data for the spectrograph profile, the ratio between the average quiet-Sun profile and the Kitt Peak near infrared atlas spectrum was calculated. Then, the absolute values of the derivative of this ratio was smoothed with a median filter. Regions with high derivatives were ignored by sorting the values and setting a cut-off limit at 57% of the values. The gaps in the curve were filled by interpolation. Finally, the ratio was decomposed into its Fourier components and restored using just eleven coefficients. The result was a smoothed spectrograph profile shown as a red curve in Fig. 4.3, by which the observed profiles are divided. Figure 4.4 shows the theoretical NIR FTS atlas profile and the corrected average profile. The corrected profile now matches the atlas profile. However, with some exceptions such as depth of spectral line cores, an indicative of stray light, and a slight shift in solar lines hinting at a negligible mismatch of the dispersion.

Ideally, the continuum of the spectral profiles should have intensity values of unity, hence all intensity profiles were normalized. Three spectral ranges were selected as continuum as these were not affected by nearby absorption lines: 1083.58 – 1083.71 nm, 1083.95 – 1084.04 nm, and 1084.13 – 1084.25 nm. The mean value of all parts of the profiles defined as continuum got calculated for all positions and afterwards all profiles got divided by the mean values to normalize all intensity profiles by the local continuum.

Since GREGOR observations are made from the ground, they need to be corrected for changes in the transparency of the atmosphere. During the observation the position of the Sun is changing,

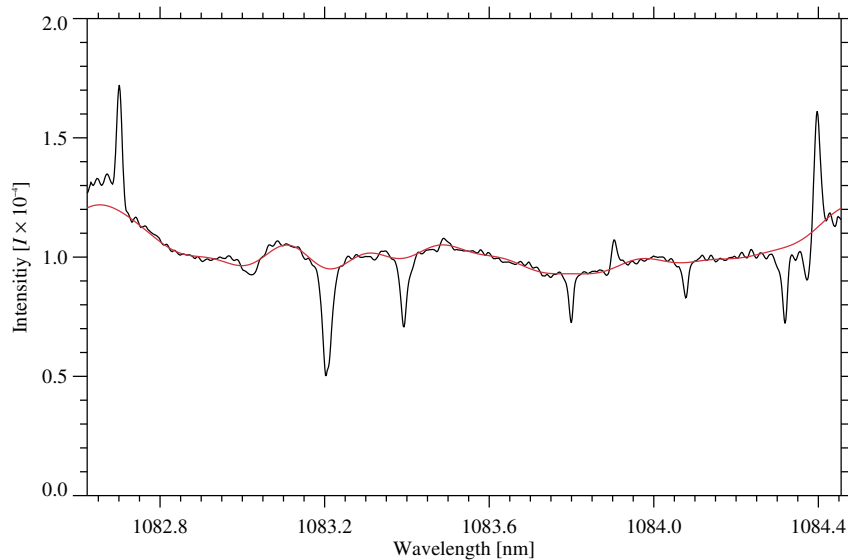


Figure 4.3: To estimate spectrograph profile the ratio (black) between observed averaged granulation profile and corresponding NIR FTS atlas was computed. This ratio was decomposed into its Fourier components. The smoothed curve (red) is restored from only eleven Fourier coefficients. The smoothed curve corresponds to the spectrograph profile used to correct the observed profiles.

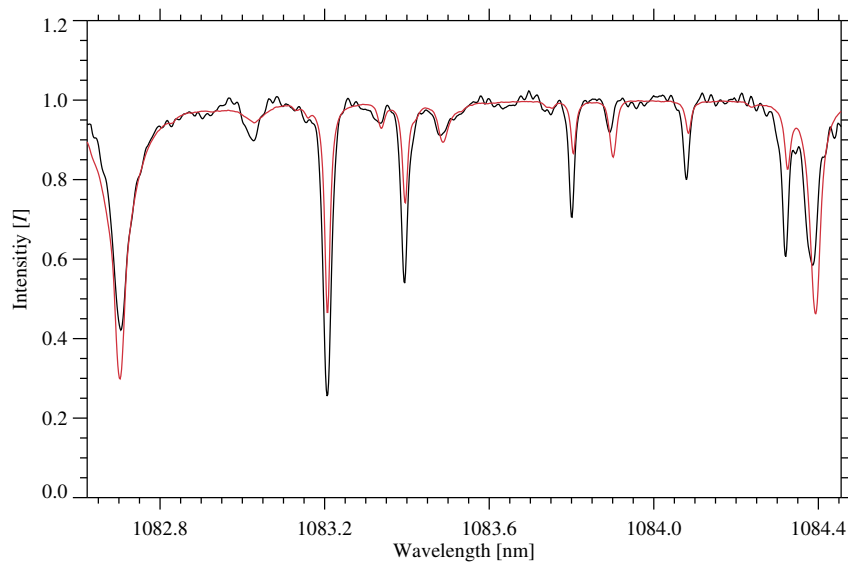


Figure 4.4: NIR FTS atlas profile (red) and averaged observed granulation profile (black) corrected for spectrograph profile shown in Fig. 4.3.

leading to a varying path length that the light has to travel through Earth’s atmosphere. Furthermore, the atmosphere itself is changing over time, including air motions and clouds. These effects are summarized as “sky transparency. To correct them, the changes in intensity over time were examined. First the mask already used before was summed over all slit positions, to get the information how many positions with granulation resided on the slit for each scan. Then, the image containing only granulation was summed over all slit positions and divided by the summed mask. This resulted in an average value for the intensity of granulation for the whole slit based on the scan number. This function was smoothed with Fourier decomposition and restoration analogously to the spectrograph profile but this time with only nine coefficients. Both the average intensity values and the smoothed function can be seen in Fig. 4.5. The profiles got divided by this smoothed function to correct variations in sky transparency.

Over the time of the observation a drift of the spectrograph occurs, which is probably caused by variations of the temperature and pressure in the spectrograph tank. This drift can easily be seen in the telluric lines. Since spectral shifts in solar lines correspond to velocities on the Sun, velocities computed from telluric lines are due to motions in Earth’s atmosphere with much lower velocities, which can be neglected. Therefore, changes in the telluric lines can be used to measure changes in the observation. To do so, a spectral range containing one telluric line was chosen, and the minimum in that range was taken as a first guess for the line core position. Afterwards, a range of ± 3 pixel around this initial position was fitted with a second order polynomial

$$I = c_2\lambda^2 + c_1\lambda + c_0. \quad (4.1)$$

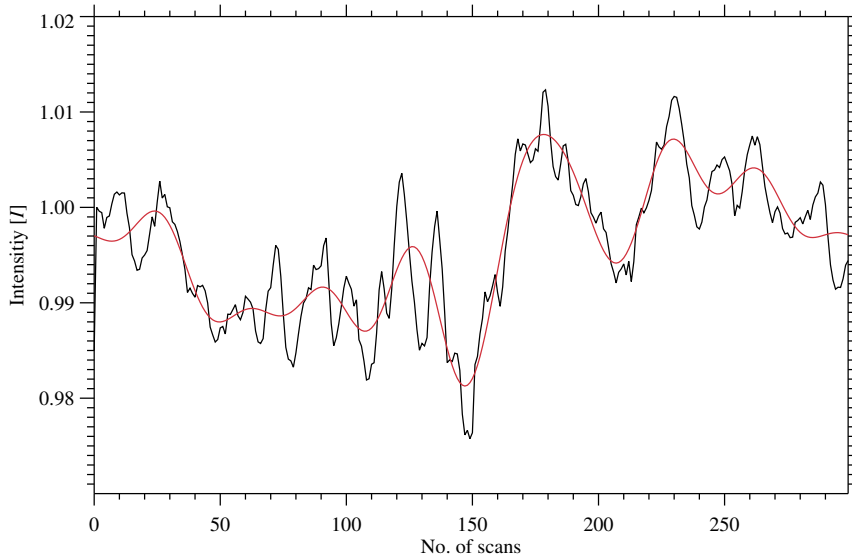


Figure 4.5: The mean variation in the intensity of granulations (black) over the 300 scan steps, which corresponds to the variation of sky transparency. This variation was decomposed into its Fourier components. The smoothed curve (red) is based on only nine Fourier coefficients. The smoothed curve was used to correct the observed profiles for the variation in sky transparency.

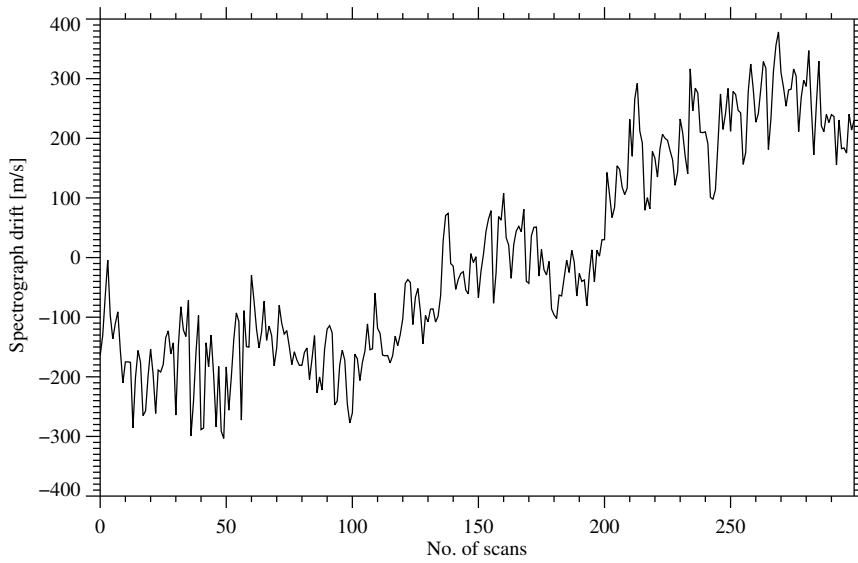


Figure 4.6: The spectrograph drift over the 300 scan steps. It was estimated using the line core position of a telluric line. The drift values are expressed as a velocity, which would affect the measured Doppler velocities.

To calculate the core position of the fit, the minimum of the function was calculated using the coefficients of the second order polynomial fit

$$\lambda_{\text{core}} = -0.5 \times \frac{c_1}{c_2}, \quad (4.2)$$

and then the respective intensity at the line core position was calculated. The mean position of the line core for all positions is computed, and then the difference between the line core position and the mean position is summed in the slit direction and divided by the number of pixels corresponding to the slit. This yields a velocity representing the spectrograph drift for every scan. The velocity per pixel was calculated using the Doppler velocity corresponding to the dispersion, i.e., the wavelength change in one pixel,

$$v = \frac{d\lambda}{\lambda} \times v_c, \quad (4.3)$$

where $d\lambda$ is the change in wavelength (dispersion multiplied by the displacement in pixels), λ is the central wavelength, and v_c is the speed of light. Figure 4.6 shows the spectrograph drift for every scan. To correct the data for the spectrograph drift, the spectra were interpolated to match the corrected spectral range.

4.2 Maps of Physical Parameters

4.2.1 Fitting Models

Several interesting physical properties can be obtained from the profiles of the spectral lines. Therefore, the observed profiles, which were normalized to the local continuum, will be fitted and the parameters of interest will be taken from these fits. An important factor for the significance of the properties is the model which is chosen for fitting. Exemplary, various fitting models were applied to the Si line. To decide how the line can be most accurately fitted, four fitting models combined with three different weightings were used. The fitting models were Gaussian, Lorentzian, Voigt, and Moffat. Line profiles can be described by various models, with different models paying respect to other aspects of the profile, in particular to the shape of the line core and the line wings. The Gaussian model is used in statistics to describe normal distributions, while the Lorentzian model represents a dampening profile. To represent the profiles of solar spectral lines, often a combination of both the Lorentzian and the Gaussian model are used. In Sect. 1.2 this combination was introduced as the Voigt model. Additionally, the Moffat model is used, which is a modified Lorentzian model. The different models are represented by the following equations, i.e.,

$$\text{Gaussian} \quad G = a_0 \cdot \exp\left(-\frac{1}{2}u^2\right) + a_3, \quad (4.4)$$

$$\text{Lorentzian} \quad L = \frac{a_0}{u^2 + 1} + a_3, \quad (4.5)$$

$$\text{Moffat} \quad M = \frac{a_0}{(u^2 + 1)^{a_4}} + a_3, \quad (4.6)$$

$$\text{and Voigt} \quad V = G * L \quad \text{profiles with} \quad (4.7)$$

$$u = \frac{x - a_1}{a_2},$$

where the symbol ‘*’ in Eq. 4.7 indicates a convolution of the two functions G and L . Parameter a_0 is the amplitude, a_1 is the peak centroid, a_2 is the half-width-at-half-minimum, a_3 is the constant representing the continuum, and a_4 is the Moffat coefficient related to the shape of the line wings.

The different weighting methods were uniform, Poisson, and Hanning weighting. As the name implies, uniform weighting treats every data point of the profile equally. Poisson weighting places emphasis on the line core, taking the distance from the line core position into account, and with increasing distance, the profile points are weighted less. Therefore, the wings of the function are still considered but with less weight than the line core. Hanning weighting also emphasis the line core, but only the core, while the wings are completely ignored. Furthermore, the fits were either constrained and unconstrained. In unconstrained fits all variables from the models are calculated, while in constrained fits some of them are set to a default value. Since the variables represent certain properties of the profile, and some of them are constants, it is reasonable to constrain them. In the constrained fits, the amplitude at the line core position was fixed, as well as the continuum, which was set to unity.

Figure 4.7 shows all different fitting models for the Si line of the average quiet-Sun profile. At first, one unconstrained fit was carried out with uniform weighting. Then three constrained fits with all weighting methods mentioned above followed. The Gaussian model is not matching well for any of the fits. Without restrictions and weightings, neither the core, nor the wings are fitted properly. Even with restrictions, the line core only gets fitted properly with Hanning weighting were the wings are completely ignored, but as expected, the wings do not match at all in this case. The Lorentzian fits are somewhat closer to the original data, but the model is still showing deficits fitting the complete line profile. Nevertheless, the line cores are already fitted sufficiently with the Lorentzian model. Although the Voigt model is a combination of Gaussian and Lorentzian profiles, there is no visible improvement compared to the Lorentzian fits. Overall, the best results were achieved with the Moffat model. Hanning weighting is the only model, that does lead to a mismatch at the wings, all other combinations lead to almost the same result.

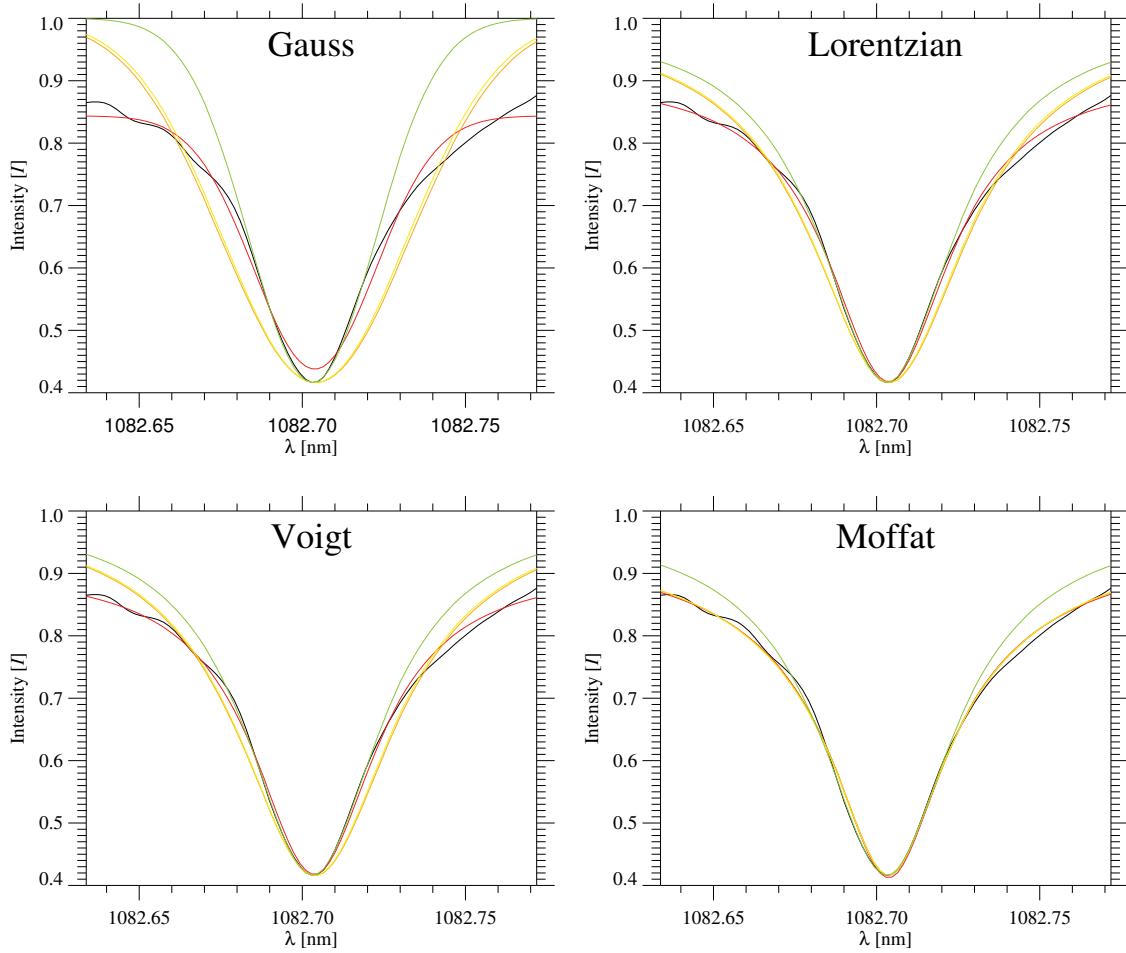


Figure 4.7: The data (black), unconstrained fit with uniform weighting (red), and constrained fits with uniform (orange), Poisson (yellow), and Hanning weighting (green).

In the end, the choice of an appropriate fitting model depends on two aspects. First, different line profiles come along with divergent properties. Discussed above is the Si line, which is a strong line with a deep line core. Therefore, to fit the complete profile, the wings have to be taken into account. Second, the choice depends on the motivation of the study. If the shape matters for further calculations, then usage of the Moffat model is needed, because it is the best model fitting the shape. But, e.g., for Doppler velocity studies, only the line core provides important information, and therefore it is not necessary to fit the wings properly.

In the following Sect. 4.2.2, maps showing physical properties are presented. When the maps were first created, fits of the Moffat model were used. While the results for the Si line were satisfying, the Ca as well as the He line were causing problems. The Ca line is magnetically sensitive, therefore, as described in Sect. 1.3.1, the line splits whenever it originates from regions containing high magnetic fields. The shape of the profile is disturbed and not fitted well with any of the models, when trying to fit the whole profile. Indeed for the strongest fields, the line splits into three components, and therefore, the profiles needed to be smoothed before being fitted. For the He line the blue and red component must be fitted separately (see Sect. 4.1.1). Even then, dark filaments often show spectral lines with two or even more components hinting at plasma at rest and fast traveling plasma within the same spatial resolution elements (either side by side or stacked on top of each other). Here, a modified fit with limited parameters was necessary. In this way, constrained Lorentzian fits with uniform weighting leads to satisfying results for all lines, but with the restriction, that only the line cores are well fitted.

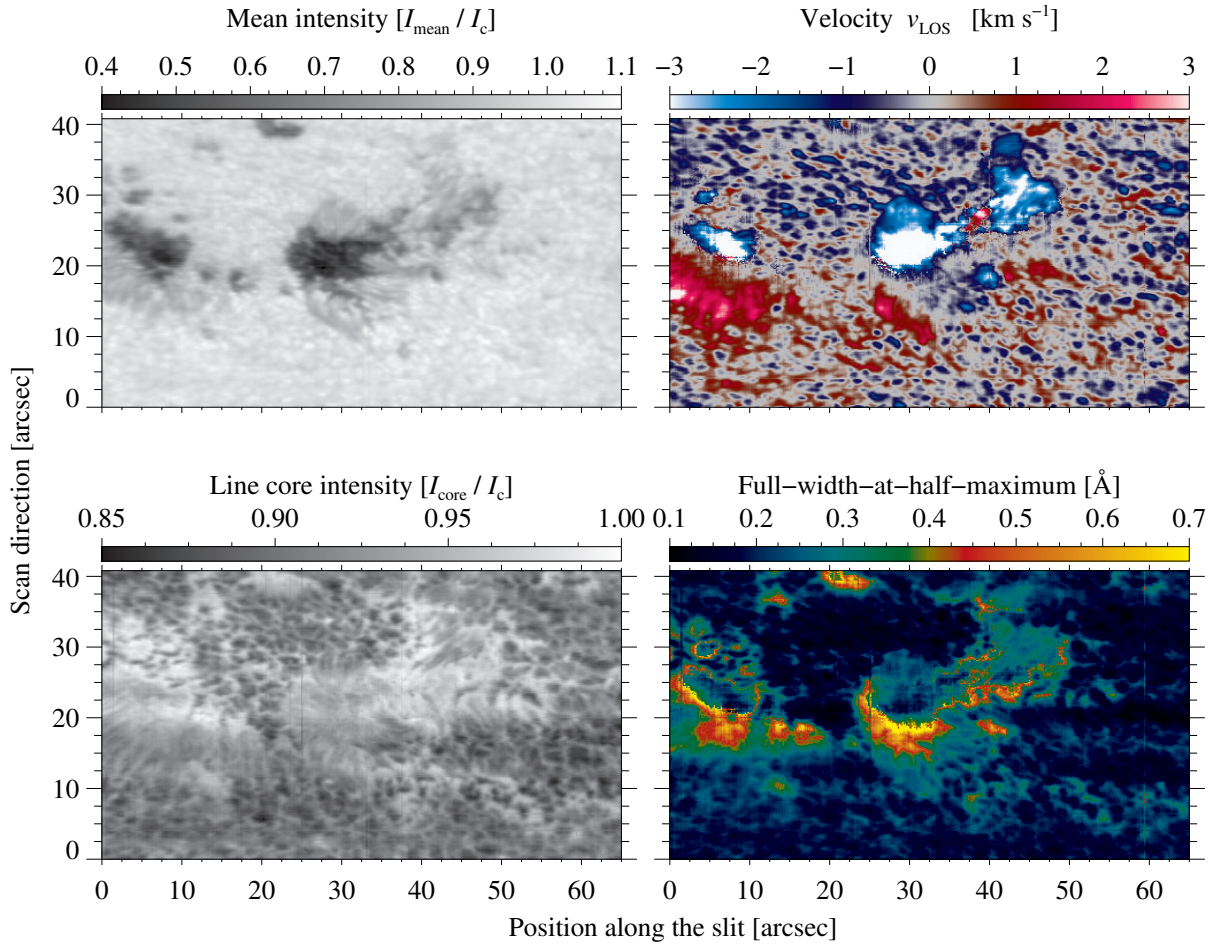


Figure 4.8: Mean intensity (top left), line core intensity (bottom left), line-of-sight velocities (top right), and full-width-at-half-maximum (bottom right) for the Ca line.

4.2.2 Physical Maps

Figures 4.8, 4.9, and 4.10 show various maps, which were created from the corrected data and the fits. This enables a detailed look at the different layers of the Sun's atmosphere. Since only the line cores are fitted properly, the maps focus on physical properties which can be extracted from the fits, without taking the wings into consideration. All figures show a continuum intensity map (top left) to visualize the locations of the sunspots umbrae and penumbrae, as well as other dark features, which can then be compared to the line specific maps.

In the panels below that (bottom left), the intensity at the line core position can be seen. The line core intensity can be derived from the coefficient a_0 of the fits, i.e., the (negative) amplitude of the profile. The maps are showing unity plus the amplitudes, which have negative values, to arrive at the intensities. All profiles were normalized by the local continuum, therefore, the maps visualize the line core intensity divided by the local continuum. Bright regions correspond to high intensities, i.e., low amplitudes, and dark regions represent low intensities, i.e., a deep line core. In magnetically sensitive lines, the line core intensity will be higher for regions with weak to moderate magnetic field strength. This phenomenon is called “line gap” (Kneer and von Uexkuell, 1991).

At the top right, maps of the Doppler velocities can be found, in which flows along the LOS are visible. Positive velocities (red) are responding to downflows, in contrast, negative velocities (blue) represent upflows. To calculate Doppler velocities Eq. 4.3 was used. In detail this means, that the wavelength of the line core is taken from the fitting parameter a_1 . The theoretical value of the line core position is then subtracted from this wavelength, and finally this value is divided by the theoretical value and multiplied by the speed of light. To extract significant values of velocities, they need to be normalized. Since the average quiet Sun should not contain any movements apart from the convective blue shift of a few 100 m s^{-1} , the mean velocity in quiet Sun regions should be close to zero (the exact

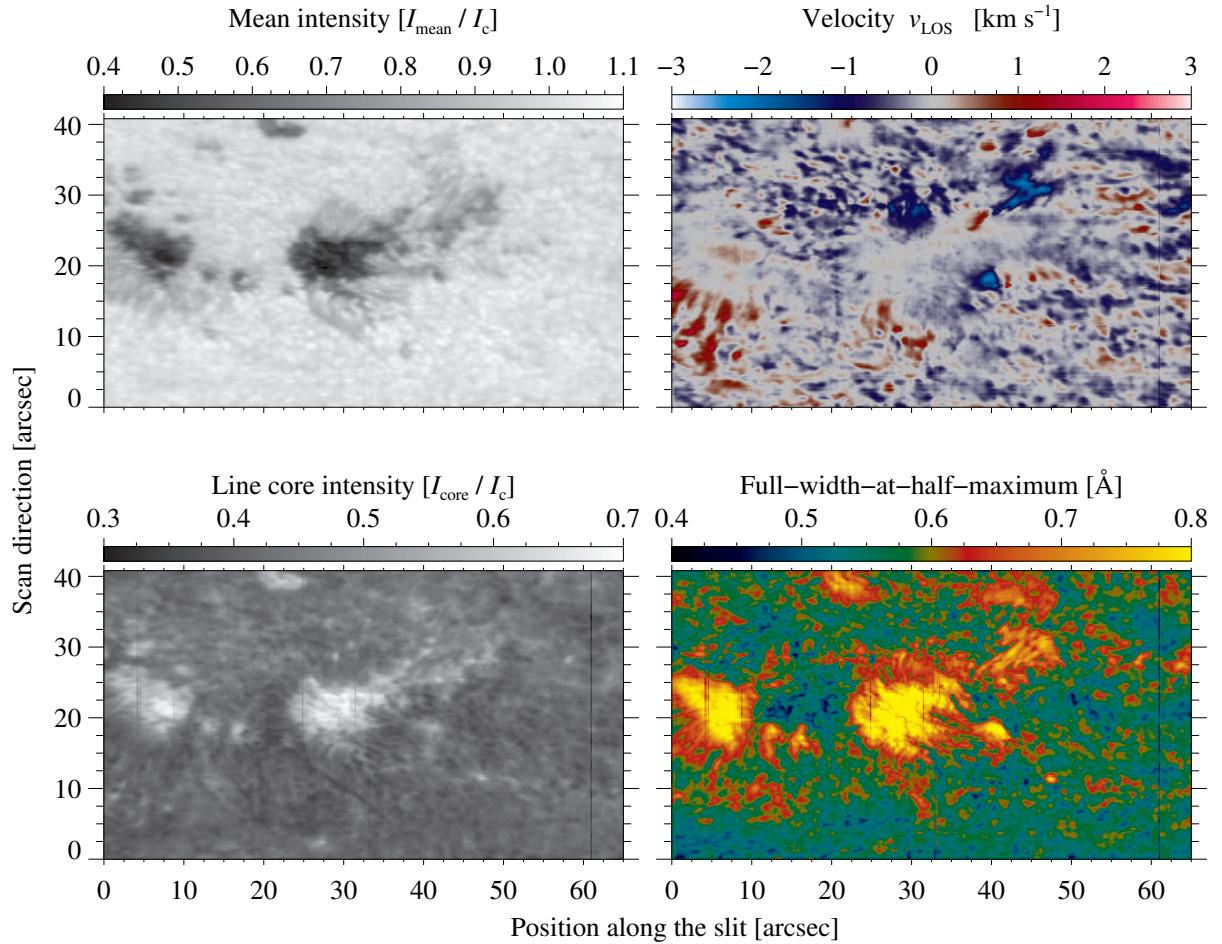


Figure 4.9: Mean intensity (top left), line core intensity (bottom left), line-of-sight velocities (top right), and full-width-at-half-maximum (bottom right) for the Si line.

value can be taken from the literature, e.g., [Balthasar \(1988\)](#)). Therefore, the mean velocity in quiet-Sun regions is calculated and subtracted from the previously computed Doppler velocities.

Often, equivalent widths are used to visualize the strength of spectral lines, but since this property represents the area the profile is covering, the wings would have to be considered, too. Thus, instead of the equivalent width, the FWHM is presented (bottom right), which is also a sufficient measure of the line broadening, and is taken from the fitting parameter a_2 . The line broadening and therefore the WFWHM is proportional to the strength of the magnetic field. Broad lines appear as bright (red-yellow), narrow lines as dark (blue) regions. The FWHM maps have been scaled by the minimum and maximum values appearing in the quiet-Sun regions in order to not display unreasonable high values which occur when the fitting failed.

Starting at the lowest atmospheric layer in which the three observed lines are formed, Fig. 4.8 depicts the properties of the Ca line, a deep photospheric line. In the velocity map as well as in the line core intensity map, the granulation pattern becomes visible. Furthermore, at the locations of both sunspots as well as the lower penumbra of the left spot, downflows are visible. In contrast, the upper penumbrae, especially the one of the right spot, shows upflows. The broadest Ca lines appear at the locations of both sunspots, but generally, broadened Ca lines are present at all locations, which show up as dark features in the mean intensity image. At the lower border of the sunspots the FWHM reaches unreasonable high values, which is hinting at the model failing at these locations. Since the Ca line exhibits Zeeman splitting in the presence of a magnetic field, the width of the Lorentz fits is not representing the observed line profile. But still, to a certain extent, the FWHM values are visualizing, where a magnetic field is present. Another phenomenon can be seen, when comparing the line core intensity with the FWHM map. At locations where the lines are broadened, the line core intensity is higher, i.e., the line is less deep. These are the above mentioned line gaps.

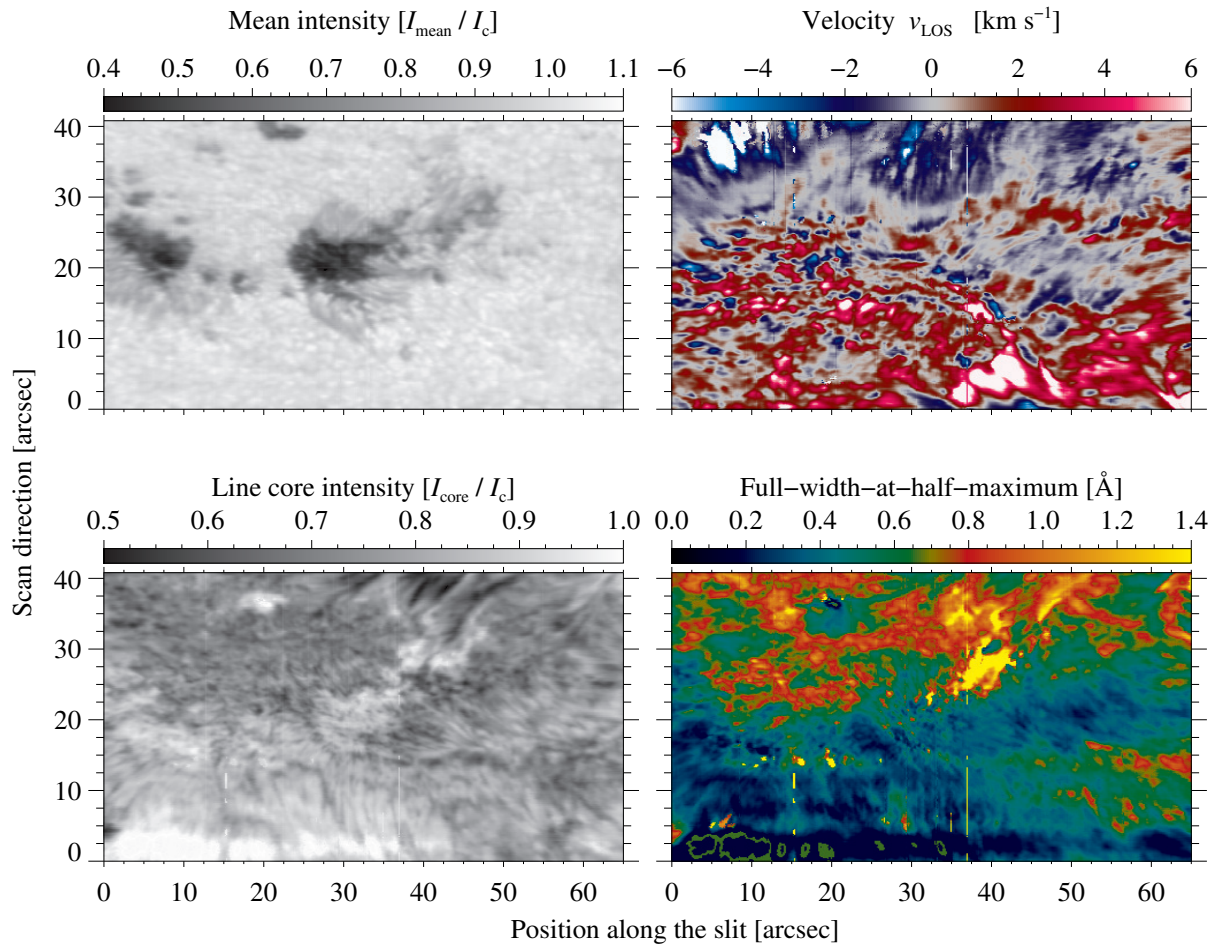


Figure 4.10: Mean intensity (top left), line core intensity (bottom left), line-of-sight velocities (top right), and full-width-at-half-maximum (bottom right) for the He line.

Next is Fig. 4.9, showing a region higher up in the photosphere, where the Si line is formed. Although they are not as clearly defined as at the bottom of the photosphere, patterns identified as granulations are evident once again. Apart from that, some up and downflows at the same locations as in the Ca Doppler maps can be seen, but they are not as distinct as in the lower photosphere. The FWHM map displays broad lines at the locations of the umbrae and medium broad lines where the penumbrae are. In the line core intensity map, once again line gaps are evident.

At last, Fig. 4.10 shows the He line, which represents the chromosphere. In the FWHM map, some artefacts can be seen in the bottom left, which hint at remaining problems, when trying to fit the He line correctly. Taking a look at the line core intensity, it is evident, that the He line was very weak in said regions. Therefore, the He line is not deep enough to be properly fitted and the values for the FWHM are unreasonable. The line core intensity and FWHM map visualize that He is mainly present in regions in the panel located above and to the right of the spots. Filamentary structures can be seen, e.g., at coordinates (40'', 40''). In the velocity maps, granulation cannot be seen anymore, but instead a plenitude of downflows in the lower half of the panel, as well as some upflows in the upper half. The upflows correspond to the dark filaments appearing in the line core intensity map.

4.2.3 Experimental Errors and Error Analysis

Working with science data and extracting physical properties from them is always subject to errors, so it is important to take them into consideration. In general there are two types, which are random and systematic errors, with the latter also including numerical ones. Random errors in principle are representing errors in the measurement, and are different when the measurement is repeated. Since this thesis focuses on observations of the Sun, the number of detected photos is very huge, and in principle

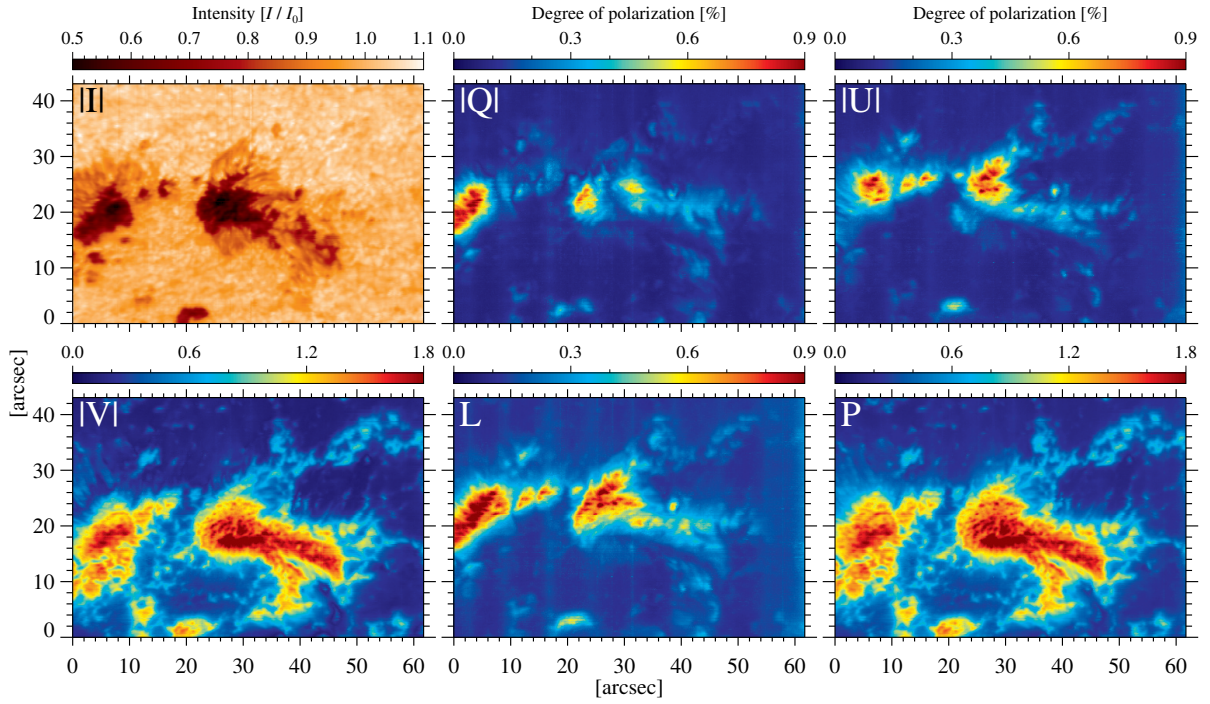


Figure 4.11: GREGOR data from the second scan at 09:24 UT with a FOV of $62'' \times 43''$ focusing on the south of the trailing part of region NOAA12396. The maps show the intensity (top left) and the degree of polarization for linear polarization (top middle), linear polarization at 45° (top right), circular polarization (bottom left), total linear polarization (bottom middle), and the total polarization (bottom right).

random errors are neglectable compared to systematic errors, but in detail, they originate from photon and readout noise. Photon noise is proportional to n^{-2} , where n is the number of detected photos. Readout noise occurs in the semiconductors of the CCD camera, as well as in the process of converting an analogue signal into a digital value. An estimation of the magnitude of random errors can be taken from the noise in the spectra presented in Fig. 4.2. While the noise in the intensities is very low compared to the depth of the spectral lines, the polarimetric data for Stokes Q and U show a higher amount of noise. The standard deviation in the regions defined as continuum for the intensities reaches 2.5% of the maximum intensity. All Stokes components reach a standard deviation of around 0.1% as degree of polarization. In Fig. 4.2 the noise seems to be different for Q, U and V, but this is only a visual effect due to the scaling. But even though the noise level is equivalent for the three components, the procentual error for the signal is different, due to the different amplitudes for the degree of polarization. For Stokes Q amplitudes do not reach values as high as for Stokes U and V and theoretically only amplitudes reaching at least three standard deviations should be considered a signal. However, the profiles shown are the sum of many observed components, which has to be taken into consideration when evaluating the signal. The response of the lines to the presence of a magnetic field is clearly visible. As a result in this study, which is focusing on the intensity profiles, the noise is negligible, but it might have to be taken into consideration when continuing the work with the polarimetric data.

Systematic errors always occur with the same values when this instrument or model is used the same way, so they are predictable and usually constant. A part of systematic errors are numerical ones, which respond to the accuracy of the algorithms and calculating accuracy of floating point variables. These errors are negligible in our study, because the results are much more influenced by the instrument and observing conditions, as well as the choice of model applied to the data. Systematic errors originating from the instrument and observation were already discussed in Sect. 4.1.2, and the data was corrected for them. As presented in Sect. 4.2.1, the choice of fitting models applied to the data is leading to the highest impacts on the properties extracted from the data. It is always important to consider, what kind of physics the model catches and therefore, which results can be taken from it, and which properties cannot be extracted from the model. This was illustrated in this thesis, by not presenting equivalent width but instead considering the FWHM as an indicator for line broadening. In the end, the results were still showing regions where the applied model failed. Regions with strong magnetic fields caused the Ca line

to be Zeeman splitted and therefore it could not be fitted appropriately. For the He line, regions with strong He absorption which contained dual flow components, as well as locations with very weak He lines led to inappropriate fits.

4.3 Outlook

Until now, only information from spectral profiles were used to obtain physical parameters. Since GRE-GOR provides spectropolarimetric data, information about the magnetic field at the target location are also evaluable. Maps showing the magnetic features of the observed region can be seen in Fig. 4.11. This first information can be taken directly from the data without further processing. When the image of the total polarization is compared to the intensity image (which is normalized to the mean continuum intensity), it is evident that magnetic structures match with the sunspots and pores locations. While regions of linear polarization are rather focused on areas close to the sunspots umbrae, circular polarization is present in large areas of the penumbrae below the umbrae.

To enhance the knowledge of the magnetic field, the next step would be to use spectral inversion techniques to obtain more detailed information. A widely used code for inversions is the Stokes inversion based on Response functions (SIR) code ([Ruiz Cobo and del Toro Iniesta, 1992](#)). SIR was developed for automated analysis and it takes all four Stokes parameters into account to determine magnetic field information. Although inversions are providing more detailed information about the magnetic field, they are very time consuming on a computer. Therefore, line fitting methods still have their merits, in particular for a first glimpse of physical processes at work in the FOV before inversions are carried out.

Chapter 5

Conclusions

In this thesis, a combination of high-resolution and synoptic observations was used to achieve a complete picture of the development of an active region. First, an introduction into the physics of sunspots was given, as well as physical properties and phenomena, which can be used to investigate structures of the Sun (Chapter 1). Then, an overview of the various instruments used for the observation at hand was presented (Chapter 2). This chapter covered SDO and IRIS, as well as GREGOR.

The main work of this thesis focused on analysing all available data to obtain information about active region NOAA 12396. Observations from space missions, i.e., SDO and IRIS were used to obtain an overview of the regions development (Chapter 3). IRIS and AIA images allowed to visualize the whole active region NOAA 12396 and revealed its structural complexity. HMI continuum images, as well as magnetograms for the whole August 6 allowed an insight of the temporal evolution of the observed region. They revealed constant changes in the appearance of the trailing part of active region NOAA 12396, especially concerning the penumbrae. The observations of [Schlichenmaier *et al.* \(2010\)](#) stating, that a steady penumbra is prevented from forming in regions of ongoing flux emergence is observed for active region NOAA 12396 as well. X-ray flux data from the GOES satellite were used to monitor the solar activity, and showed that while active region NOAA 12396 made a prominent contribution to the solar activity, there were no major flares at the times of the GREGOR observations.

Ground based observations from GRIS provided spectropolarimetric data, which was carefully corrected and analysed to acquire the main results of this thesis (Chapter 4). At first, a general overview is given about what information the data contains. Then, the main part of the analysis started with applying corrections, including the spectrograph profile, sky transparency and the spectrograph drift corrections. To the corrected data various combinations of fitting models and weightings were executed to allow statements of how to fit the spectral profiles appropriately. Here, various factors were discussed which have to be taken into consideration when fitting line profiles. After applying the Moffat model to the data, which seemed to be the most fitting for one spectral line, problems occurred when it was applied to another line profile. Both Zeeman splitting of the Ca line and the two components of the He line disrupted the fitting. Finally, physical parameters, such as the line core intensity, Doppler velocities, and FWHM were extracted from the fitting parameters and visualized in maps for all three observed spectral lines. This allowed a view into different atmospheric layers of the Sun, i.e., the bottom of the photosphere represented by the Ca line, the upper photosphere, where the Si line originates, and finally the chromosphere, where the He line forms.

This study would have continued with evaluating the polarimetric data provided by GRIS, but within this thesis, only a short outlook concerning these data could be given. The data contain information about the magnetic field itself, while the previously presented data only contained hints at magnetic activity, e.g., when line broadening was observed. But this thesis already shows, how much information can be extracted from observations, where ground-based data and observations from space missions are coordinated. Active regions are complex phenomena of the Sun and only the combination of high-resolution and synoptic observations allow a complete and deep analysis of their physics.

Bibliography

- Abetti, G.: 1957, *The Sun.*, Faber and Faber, London.
- Avrett, E.H., Fontenla, J.M., Loeser, R.: 1994, Formation of the Solar 10830 Ångström Line. In: Rabin, D.M., Jefferies, J.T., Lindsey, C. (eds.) *Infrared Solar Physics, IAU Symp.* **154**, 35.
- Balthasar, H.: 1988, The center-to-limb variation of solar spectral lines. *Astron. Astrophys.* **72**, 473.
- Bentley, R.D., Freeland, S.L.: 1998, SOLARSOFT – An Analysis Environment for Solar Physics. In: *Crossroads for European Solar and Heliospheric Physics. Recent Achievements and Future Mission Possibilities, ESA Spec. Publ.* **417**, 225.
- Berger, T.E., Berdyugina, S.V.: 2003, The Observation of Sunspot Light-Bridge Structure and Dynamics. *Astrophys. J., Lett.* **589**, L117. [DOI](#).
- Berkefeld, T., Schmidt, D., Soltau, D., von der Lühe, O., Heidecke, F.: 2012, The GREGOR Adaptive Optics System. *Astron. Nachr.* **333**, 863. [DOI](#).
- Carroll, B.W., Ostlie, D.A.: 2007, *An Introduction to Modern Astrophysics*, Pearson Education, publishing as Addison-Wesley, San Francisco.
- Collados, M., Lagg, A., Díaz Garcí A, J.J., Hernández Suárez, E., López López, R., Páez Mañá, E., Solanki, S.K.: 2007, Tenerife Infrared Polarimeter II. In: Heinzel, P., Dorotovič, I., Rutten, R.J. (eds.) *The Physics of Chromospheric Plasmas, ASP Conf. Ser.* **368**, 611.
- Collados, M., López, R., Páez, E., Hernández, E., Reyes, M., Calcines, A., et.al.: 2012, GRIS: The GREGOR Infrared Spectrograph. *Astron. Nachr.* **333**, 872. [DOI](#).
- de Pontieu, B., Title, A.M., Lemen, J.R., Kushner, G.D., Akin, D.J., Allard, B., et.al.: 2014, The Interface Region Imaging Spectrograph (IRIS). *Sol. Phys.* **289**, 2733. [DOI](#).
- Degenhardt, D., Lites, B.W.: 1993a, The Magnetohydrodynamics of Umbral Flux Tubes. I. Theoretical Model. *Astrophys. J.* **404**, 383. [DOI](#).
- Degenhardt, D., Lites, B.W.: 1993b, The Magnetohydrodynamics of Umbral Flux Tubes. II. Spectroscopic Properties. *Astrophys. J.* **416**, 875. [DOI](#).
- Denker, C., Lagg, A., Puschmann, K.G., Schmidt, D., Schmidt, W., Sobotka, M., et.al.: 2012, The GREGOR Solar Telescope. *IAU Special Session* **6**, 203.
- Domingo, V., Fleck, B., Poland, A.I.: 1995, The SOHO Mission: An Overview. *Sol. Phys.* **162**, 1. [DOI](#).
- Evershed, J.: 1909a, Radial Movement in Sun-Spots. *Mon. Not. R. Astron. Soc.* **69**, 454.
- Evershed, J.: 1909b, Radial Movement in Sunspots. *Kodaikanal Obs. Bull.* **2**, 63.
- Foukal, P.: 2013, *Solar Astrophysics*, Wiley-VCH, Weinheim.
- Freeland, S.L., Handy, B.N.: 1998, Data Analysis with the SolarSoft System. *Sol. Phys.* **182**, 497.
- Golub, L.: 1980, X-ray Bright Points and the Solar Cycle. *Phil. Trans. R. Soc. London Ser. A* **297**, 595. [DOI](#).

- González Manrique, S.J., Kuckein, C., Pastor Yabar, A., Collados, M., Denker, C., Fischer, C.E., et.al.: Fitting Peculiar Spectral Profiles in He I 10830 Å Absorption Features. *Astron. Nachr.* in press.
- Hale, G.E.: 1908, On the Probable Existence of a Magnetic Field in Sun-Spots. *Astrophys. J.* **28**, 315. [DOI](#).
- Hale, G.E., Nicholson, S.B.: 1925, The Law of Sun-Spot Polarity. *Astrophys. J.* **62**, 270. [DOI](#).
- Hale, G.E., Ellerman, F., Nicholson, S.B., Joy, A.H.: 1919, The Magnetic Polarity of Sun-Spots. *Astrophys. J.* **49**, 153. [DOI](#).
- Handy, B.N., Acton, L.W., Kankelborg, C.C., Wolfson, C.J., Akin, D.J., Bruner, M.E., et.al.: 1999, The Transition Region and Coronal Explorer. *Sol. Phys.* **187**, 229. [DOI](#).
- Hathaway, D.H.: 2015, The Solar Cycle. *Living Rev. Sol. Phys.* **12**. [DOI](#).
- Hofmann, A., Arlt, K., Balthasar, H., Bauer, S.M., Bittner, W., Paschke, J., et.al.: 2012, The GREGOR Polarimetric Calibration Unit. *Astron. Nachr.* **333**, 854. [DOI](#).
- Kinman, T.D.: 1952, Motions in the Sun at the Photospheric Level. II. Evershed Effect in Sunspot No. 9987, Mt. Wilson. *Mon. Not. R. Astron. Soc.* **112**, 425.
- Kitai, R., Watanabe, H., Nakamura, T., Otsuji, K.-I., Matsumoto, T., Ueno, S., et.al.: 2007, Umbral Fine Structures in Sunspots Observed with Hinode Solar Optical Telescope. *Publ. Astron. Soc. Jpn.* **59**, 585. [DOI](#).
- Kneer, F.: 2012, Hopes and Expectations with GREGOR. *Astron. Nachr.* **333**, 790. [DOI](#).
- Kneer, F., von Uexkuell, M.: 1991, On the Structure of Spectral Line Gap Regions. *Astron. Astrophys.* **247**, 556.
- Kneer, F., Wiehr, E.: 1989, The Gregory-Coudé- Telescope at the Observatorio Del Teide Tenerife. In: Rutten, R.J., Severino, G. (eds.) *Solar and Stellar Granulation, NATO Advanced Science Institutes (ASI) Series C* **263**, 13.
- Kosugi, T., Matsuzaki, K., Sakao, T., Shimizu, T., Sone, Y., Tachikawa, S., et.al.: 2007, The Hinode (Solar-B) Mission: An Overview. *Sol. Phys.* **243**, 3. [DOI](#).
- Kuckein, C., Martínez Pillet, V., Centeno, R.: 2012, An Active Region Filament Studied Simultaneously in the Chromosphere and Photosphere. I. Magnetic Structure. *Astron. Astrophys.* **539**, A131. [DOI](#).
- Leka, K.D., Skumanich, A.: 1998, The Evolution of Pores and the Development of Penumbrae. *Astrophys. J.* **507**, 454. [DOI](#).
- Lemen, J.R., Title, A.M., Akin, D.J., Boerner, P.F., Chou, C., Drake, J.F., et.al.: 2012, The Atmospheric Imaging Assembly (AIA) on the Solar Dynamics Observatory (SDO). *Sol. Phys.* **275**, 17. [DOI](#).
- Louis, R.E., Puschmann, K.G., Kliem, B., Balthasar, H., Denker, C.: 2014, Sunspot Splitting Triggering an Eruptive Flare. *Astron. Astrophys.* **562**, A110. [DOI](#).
- Márquez, I., Sánchez Almeida, J., Bonet, J.A.: 2006, High-Resolution Proper Motions in a Sunspot Penumbra. *Astrophys. J.* **638**, 553. [DOI](#).
- Martínez Pillet, V., Collados, M., Sánchez Almeida, J., González, V., Cruz-Lopez, A., Manescau, A., et.al.: 1999, LPSP & TIP: Full Stokes Polarimeters for the Canary Islands Observatories. In: Rimmele, T.R., Balasubramaniam, K.S., Radick, R.R. (eds.) *High Resolution Solar Physics: Theory, Observations, and Techniques, ASP Conf. Ser.* **183**, 264.
- Maunder, E.W.: 1890, Professor Spoerer's Researches on Sun-spots. *Mon. Not. R. Astron. Soc.* **50**, 251.

- Mullan, D.J.: 2010, *Physics of the Sun: A First course* **CRC Series in Pure and Applied Physics**, Boca Raton, Florida.
- Muller, R.: 1973, Étude Morphologique et Cinématique des Structures Fines d'une Tache Solaire. *Sol. Phys.* **29**, 55. [DOI](#).
- Newton, H.W.: 1955, The Lineage of the Great Sunspots. *Vistas Astron.* **1**, 666. [DOI](#).
- Pesnell, W.D., Thompson, B.J., Chamberlin, P.C.: 2012, The Solar Dynamics Observatory (SDO). *Sol. Phys.* **275**, 3. [DOI](#).
- Petrovay, K., van Driel-Gesztelyi, L.: 1997, Making Sense of Sunspot Decay. I. Parabolic Decay Law and Gnevyshev-Waldmeier Relation. *Sol. Phys.* **176**, 249. [DOI](#).
- Podgorski, W.A., Cheimets, P.N., Golub, L., Lemen, J.R., Title, A.M.: 2012, Design, Performance Prediction, and Measurements of the Interface Region Imaging Spectrograph (IRIS) Telescope. In: Takahashi, T., Murray, S.S., den Herder, J.-W.A. (eds.) *Space Telescopes and Instrumentation 2012: Ultraviolet to Gamma Ray, Proceedings of SPIE* **8443**, 3. [DOI](#).
- Roupe van der Voort, L.H.M., Löfdahl, M.G., Kiselman, D., Scharmer, G.B.: 2004, Penumbra Structure at 0.1 arcsec Resolution. I. General Appearance and Power Spectra. *Astron. Astrophys.* **414**, 717. [DOI](#).
- Rüedi, I., Solanki, S.K., Livingston, W.C.: 1995, Infrared Lines as Probes of Solar Magnetic Features. X. HeI 10830A as a Diagnostic of Chromospheric Magnetic Fields. *Astron. Astrophys.* **293**.
- Ruiz Cobo, B., del Toro Iniesta, J.C.: 1992, Inversion of Stokes Profiles. *Astrophys. J.* **398**, 375. [DOI](#).
- Scherrer, P.H., Bogart, R.S., Bush, R.I., Hoeksema, J.T., Kosovichev, A.G., Schou, J., *et al.*: 1995, The Solar Oscillations Investigation – Michelson Doppler Imager. *Sol. Phys.* **162**, 129. [DOI](#).
- Scherrer, P.H., Schou, J., Bush, R.I., Kosovichev, A.G., Bogart, R.S., Hoeksema, J.T., *et al.*: 2012, The Helioseismic and Magnetic Imager (HMI) Investigation for the Solar Dynamics Observatory (SDO). *Sol. Phys.* **275**, 207. [DOI](#).
- Schlichenmaier, R., Collados, M.: 2002, Spectropolarimetry in a Sunspot Penumbra. Spatial Dependence of Stokes Asymmetries in Fe I 1564.8 nm. *Astron. Astrophys.* **381**, 668. [DOI](#).
- Schlichenmaier, R., Rezaei, R., Bello González, N., Waldmann, T.A.: 2010, The Formation of a Sunspot Penumbra. *Astron. Astrophys.* **512**, L1. [DOI](#).
- Schmidt, W., von der Lühe, O., Volkmer, R., Denker, C., Solanki, S.K., Balthasar, H., *et al.*: 2012, The 1.5 Meter Solar Telescope GREGOR. *Astron. Nachr.* **333**, 796. [DOI](#).
- Schou, J., Scherrer, P.H., Bush, R.I., Wachter, R., Couvidat, S., Rabello-Soares, M.C., *et al.*: 2012, Design and Ground Calibration of the Helioseismic and Magnetic Imager (HMI) Instrument on the Solar Dynamics Observatory (SDO). *Sol. Phys.* **275**, 229. [DOI](#).
- Schwabe, M.: 1843, Die Sonne. *Astron. Nachr.* **20**, 283. [DOI](#).
- Sobotka, M., Hanslmeier, A.: 2005, Photometry of Umbral Dots. *Astron. Astrophys.* **442**, 323. [DOI](#).
- Sobotka, M., Bonet, J.A., Vazquez, M.: 1993, A High-Resolution Study of Inhomogeneities in Sunspot Umbrae. *Astrophys. J.* **415**, 832. [DOI](#).
- Sobotka, M., Brandt, P.N., Simon, G.W.: 1997, Fine Structure in Sunspots. I. Sizes and Lifetimes of Umbral Dots. *Astron. Astrophys.* **328**, 682.
- Solanki, S.K., Walther, U., Livingston, W.: 1993, Infrared Lines as Probes of Solar Magnetic Features. VI. The Thermal-Magnetic Relation and Wilson Depression of a Simple Sunspot. *Astron. Astrophys.* **277**, 639.

- St. John, C.E.: 1913, Radial Motion in Sun-Spots. *Astrophys. J.* **37**, 322. [DOI](#).
- Stix, M.: 2002, *The Sun: An Introduction*, Springer, Berlin. [DOI](#).
- Thomas, J.H., Weiss, N.O.: 2008, *Sunspots and Starspots, Cambridge Astrophysics Series*, Cambridge University Press, New York.
- Tritschler, A., Schmidt, W.: 2002, Sunspot Photometry with Phase Diversity. II. Fine-Structure Characteristics. *Astron. Astrophys.* **388**, 1048. [DOI](#).
- Trujillo Bueno, J., Landi Degl’Innocenti, E., Collados, M., Merenda, L., Manso Sainz, R.: 2002, Selective Absorption Processes as the Origin of Puzzling Spectral Line Polarization from the Sun. *Nature* **415**, 403.
- Vazquez, M.: 1973, A Morphological Study of the Light-Bridges in Sunspots. *Sol. Phys.* **31**, 377. [DOI](#).
- Wallace, L., Hinkle, K., Livingston, W.C.: 1993, *An Atlas of the Photospheric Spectrum from 8900 to 13600 cm⁻¹ (7350 to 11230 Ångströms)*.
- Wilson, A.: 1769, Observations of the Transit of Venus Over the Sun, Contained in a Letter to the Reverend Nevil Maskelyne, Astronomer Royal, from Dr. Alexander Wilson, Professor of Astronomy in the University of Glasgow. *Phil. Trans. R. Soc. London Ser. A* **59**, 333.
- Woods, T.N., Eparvier, F.G., Hock, R., Jones, A.R., Woodraska, D., Judge, D., et.al.: 2012, Extreme Ultraviolet Variability Experiment (EVE) on the Solar Dynamics Observatory (SDO): Overview of Science Objectives, Instrument Design, Data Products, and Model Developments. *Sol. Phys.* **275**, 115. [DOI](#).
- Yang, G., Xu, Y., Wang, H., Denker, C.: 2003, High Spatial Resolution Observations of Pores and the Formation of a Rudimentary Penumbra. *Astrophys. J.* **597**, 1190. [DOI](#).
- Zirin, H.: 1972, Fine Structure of Solar Magnetic Fields. *Sol. Phys.* **22**, 34. [DOI](#).
- Zirker, J.B.: 2002, *Journey from the Center of the Sun*, Princeton University Press, New Jersey.
- Zwaan, C.: 1968, The Structure of Sunspots. *Ann. Rev. Astron. Astrophys.* **6**, 135. [DOI](#).
- Zwaan, C.: 1987, Elements and Patterns in the Solar Magnetic Field. *Ann. Rev. Astron. Astrophys.* **25**, 83. [DOI](#).
- Zwaan, C.: 1992, The Evolution of Sunspots. In: Thomas, J.H., Weiss, N.O. (eds.) *In Sunspots: Theory and Observations*, *NATO ASI Ser. C* **375**, 75.

Acknowledgments

I would like to express my sincere appreciation to my supervisor Prof. Dr. Marek Kowalski, who always trusted in my work and a great thanks for all his efforts. Furthermore, my deepest gratitude to my co-supervisor apl. Prof. Dr. Carsten Denker, who took me into his group for this thesis. Without his trust, support and wonderful attitude I would have never been able to write this thesis. I could not have wished for a better co-supervisor and working environment.

It was a pleasure to work with the Optical Solar Physics group at AIP. I want to say my great thanks to Dr. Meetu Verma, with whom I worked during all the course of this thesis. I always enjoyed working with you and felt supported encouraged to write this thesis. Also thanks for all the comments and suggestions, as well as your friendly attitude. Furthermore, I would like to express my thanks to Andrea Diercke, Linh Le Phuong, Dr. Christoph Kuckein, Sergio J. González Manrique, and Dr. Horst Balthasar for their support and company. You made me feel welcome from the very first day, and I am really proud that I was allowed to work as part of your group.

Special thanks to my parents, Angelika and Jürgen Böhm, who supported and encouraged me during my whole studying. Also, to my dear sister Patricia and her boyfriend Tilo Kastner for boosting my self-confidence by always believing in me, whenever I needed it the most. Furthermore a want to thank Astrid Kastner for having an open ear to my worries, and for helping me to focus. Finally, a great thanks to my dearest friend Florian Meyl for listening to me even in the middle of night and for motivating me whenever needed.

I would like to thank all the people involved in providing solar observational data. The data used for this thesis was was obtained by the observatories and instruments in the acknowledgments below. The 1.5-meter GREGOR solar telescope was build by a German consortium under the leadership of the Kiepenheuer-Institut für Sonnenphysik in Freiburg with the Leibniz-Institut für Astrophysik Potsdam, the Institut für Astrophysik Göttingen, and the Max-Planck-Institut für Sonnensystemforschung in Göttingen as partners, and with contributions by the Instituto de Astrofísica de Canarias and the Astronomical Institute of the Academy of Sciences of the Czech Republic. SDO HMI and AIA data are provided by the Joint Science Operations Center – Science Data Processing. IRIS is a NASA Small Explorer mission developed and operated by LMSAL with mission operations executed at NASA ARC and major contributions to downlink communications funded by the NSC (Norway). NSO/Kitt Peak FTS data used here were produced by NSF/NOAO. The GOES X-ray flux measurements were made available by the National Geophysical Data Center.

Appendix A – List of Acronyms

AIA	Atmospheric Imaging Assembly
AIP	Leibniz-Institut für Astrophysik Potsdam
CCD	Charge-coupled device
EVE	Extreme Ultraviolet Variability Experiment
FLC	ferroelectric crystal
FOV	field-of-view
FUV	far ultraviolet
FWHM	full-width-at-half-maximum
GOES	Geostationary Operational Environmental Satellite
GCT	Gregory-Coudé Telescope
GPU	GREGOR Polarimetric Unit
GRIS	GREGOR Infrared Spectrograph
HMI	Helioseismic and Magnetic Imager
IAG	Institut für Astrophysik Göttingen
IRIS	Interface Region Imaging Spectrograph
KIS	Kiepenheuer-Institut für Sonnenphysik
LOS	line-of-sight
LWS	Living with a Star
MDI	Michelson Doppler Imager
MPS	Max-Planck-Institut für Sonnensystemforschung
NASA	National Aeronautics and Space Administration
NIST	National Institute of Standards and Technology
NOAA	National Oceanic and Atmospheric Administration
NUV	Near ultraviolet
ROI	region-of-interest
SDO	Solar Dynamics Observatory
SIR	Stokes inversion based on Response functions
SoHO	Solar and Heliospheric Observatory
TIP-II	Tenerife Infrared Polarimeter-II
TRACE	Transition Region and Coronal Explorer
UT	Universal Time
UV	ultraviolet
VTT	Vacuum Tower Telescope

Appendix B – Programs used to create the figures

Chapter 1

Tab. 1.1: Table with all images created by myself.

Chapter 3

- Fig. 3.1: Template provided by Meetu Verma, used with minor modifications.
- Fig. 3.2: Template provided by Meetu Verma, used with minor modifications.
- Fig. 3.3: Template provided by Meetu Verma, modified to create a figure with the desired number of panels and time periods.
- Fig. 3.4: Template provided by Meetu Verma, used with minor modifications.

Chapter 4

- Fig. 4.1: Program written by myself.
- Fig. 4.2: Program written by myself.
- Figs. 4.3, 4.4, 4.5, and 4.6: The program to correct the data was written by Meetu Verma. Using the corrected data, a program written by myself was used to illustrate the corrections.
- Fig. 4.7: Parts of a fitting program by Meetu Verma were used for a modified version to apply the fits to averaged profiles and creating the figure.
- Figs. 4.8, 4.9, and 4.10: Parts of a program from Meetu Verma were adapted to create programs for the three maps calculating the desired properties and creating the figures.
- Fig. 4.11: Program written by myself.

For all programs IDL bibliographies were used, the most important being SolarSoft ([Bentley and Freeland, 1998](#); [Freeland and Handy, 1998](#)). All other sources for images are cited in the captions.

Eigenständigkeitserklärung

Hiermit versichere ich, dass ich die vorliegende Arbeit selbständig verfasst und keine anderen als die angegebenen Quellen und Hilfsmittel verwendet habe.

Berlin, 4. Mai 2016

Felicitas Böhm